Available online at www.sciencedirect.com

ScienceDirect

Geochimica et Cosmochimica Acta 164 (2015) 127–145

Geochimica et Cosmochimica Acta

www.elsevier.com/locate/gca

The effect of pH, grain size, and organic ligands on biotite weathering rates

Andrew W. Bray [a,b,*], Eric H. Oelkers [b,c], Steeve Bonneville [a,d], Domenik Wolff-Boenisch [e,f], Nicola J. Potts [a,g], Gary Fones [h], Liane G. Benning [a,i]

[a] Cohen Geochemistry, School of Earth and Environment, University of Leeds, LS2 9JT, United Kingdom
[b] Géochimie et Biogéochimie Expérimentale, GET CNRS, UMR 5563, 14 av. Edouard Belin, 31400 Toulouse, France
[c] Department of Earth Sciences, University College London, Gower Street, London WC1E 6BT, United Kingdom
[d] Biogéochimie et Modélisation du Système Terre, Département des Sciences de la Terre et de l'Environnement, Université Libre de Bruxelles, 50 av. F. D. Roosevelt, 1050 Brussels, Belgium
[e] Institute of Earth Sciences, University of Iceland, Sturlugata 7, 101 Reykjavik, Iceland
[f] Department of Applied Geology, Curtin University, GPO Box U1987, Perth, 6845 Western Australia, Australia
[g] Department of Physical Sciences, The Open University, Walton Hall, Milton Keynes MK7 6AA, United Kingdom
[h] School of Earth and Environmental Sciences, University of Portsmouth, PO1 3QL, United Kingdom
[i] GFZ, German Research Centre for Geosciences, Telegrafenberg, Potsdam 14473, Germany

Received 10 October 2014; accepted in revised form 13 April 2015; Available online 7 May 2015

Abstract

Biotite dissolution rates were determined at 25 °C, at pH 2–6, and as a function of mineral composition, grain size, and aqueous organic ligand concentration. Rates were measured using both open- and closed-system reactors in fluids of constant ionic strength. Element release was non-stoichiometric and followed the general trend of Fe, Mg > Al > Si. Biotite surface area normalised dissolution rates (r_i) in the acidic range, generated from Si release, are consistent with the empirical rate law:

$$r_i = k_{H,i} a_{H^+}^{xi}$$

where $k_{H,i}$ refers to an apparent rate constant, a_{H^+} designates the activity of protons, and x_i stands for a reaction order with respect to protons. Rate constants range from 2.15×10^{-10} to 30.6×10^{-10} ($moles_{biotite}\ m^{-2}\ s^{-1}$) with reaction orders ranging from 0.31 to 0.58. At near-neutral pH in the closed-system experiments, the release of Al was stoichiometric compared to Si, but Fe was preferentially retained in the solid phase, possibly as a secondary phase. Biotite dissolution was highly spatially anisotropic with its edges being ~120 times more reactive than its basal planes. Low organic ligand concentrations slightly enhanced biotite dissolution rates. These measured rates illuminate mineral–fluid–organism chemical interactions, which occur in the natural environment, and how organic exudates enhance nutrient mobilisation for microorganism acquisition.

1. INTRODUCTION

The weathering of silicate minerals controls the chemical composition of natural waters, supplies nutrients to the biosphere and, over geological time-scales, weathering is a crucial regulatory process of the global carbon cycle (Berner and Berner, 1996). Among silicates, the weathering of

* Corresponding author at: Cohen Geochemistry, School of Earth and Environment, University of Leeds, LS2 9JT, United Kingdom.
E-mail address: a.w.bray@leeds.ac.uk (A.W. Bray).

http://dx.doi.org/10.1016/j.gca.2015.04.048
0016-7037/

phyllosilicates has a particularly strong influence on geochemical cycles due to their abundance, large specific surface areas, and high ion-exchange capacities (Sposito, 1984; Davis and Kent, 1990; Drever, 1997; Bowser and Jones, 2002). Among phyllosilicates, biotite is the key source of primary (K) and secondary (Fe, Mg, Al) nutrients in soils and freshly exposed rocks, particularly in Boreal regions. Overall, it has been estimated that biotite makes up ~7% of the exposed crustal surface (Nesbitt and Young, 1984). During the past few decades, many field and laboratory studies have shown that the biosphere is crucial in controlling mineral weathering and therefore influencing geochemical processes (Beerling and Berner, 2005; Taylor et al., 2009), yet often a validation of the magnitude of these processes is lacking.

For biotite, a number of experimental studies quantifying its abiotic dissolution have revealed that at a given pH, the dissolution rates can vary by up to 1.5 orders of magnitude (Acker and Bricker, 1992; Turpault and Trotignon, 1994; Kalinowski and Schweda, 1996; Malmström et al., 1996; Malmström and Banwart, 1997; He et al., 2005). From studying other mineral systems, these variations may be explained by several possible factors; (a) differences and variations in bulk chemical composition, (b) differences in particle size and geometry, (c) differences in experimental approaches or durations, and (d) variations in chemical compositions and concentrations of the experimental fluids (Oelkers et al., 2001; Brantley, 2003; Köhler et al., 2005; Schott et al., 2009; Zhang and Lüttge, 2009; Arvidson and Lüttge, 2010; Fischer et al., 2014; Rimstidt, 2014). The purpose of this study is to document how each of these factors affects biotite dissolution.

Biotite is a subgroup of the mica mineral group, which forms a solid solution series with iron and magnesium end members annite ($K\,Fe_3\,AlSi_3O_{10}\,(OH)_2$) and phlogopite ($K\,Mg_3\,AlSi_3O_{10}\,(OH)_2$). The variable concentrations of Fe and Mg in natural biotite samples, in conjunction with the substitution of a wide variety of other elements in the octahedral and tetrahedral silicate sheets, may lead to differences in element release rates when normalised to the biotite formula. Therefore, to test the effect of mineral composition on dissolution rates, we present here data from the dissolution of two chemically distinct biotite samples.

Moreover, biotite is highly anisotropic in terms of surface reactivity, with edge ($hk0$) surfaces being between 30 and 300 times more reactive than basal (001) surfaces (Turpault and Trotignon, 1994; Hodson, 2006). This implies that grain shape and size play a crucial role in measuring and interpreting dissolution rate data. Surprisingly however, the majority of published biotite dissolution rates are normalised to the total surface area, and the effect of geometric anisotropy on reactivity has not been addressed experimentally. Therefore, in this study, we present data from experiments performed with three different biotite size fractions, each with distinct geometric (edge to basal surface) ratios to better understand the control of grain size and geometry on biotite dissolution kinetics.

Existing biotite dissolution kinetic studies have employed a variety of experimental approaches. These include (a) open-system experiments performed in fluidized-bed reactors and flow-through columns (Acker and Bricker, 1992), dialysis-cell reactors (Kalinowski and Schweda, 1996), thin-film flow-through reactors (Malmström et al., 1996; Malmström and Banwart, 1997), and continuous-flow reactors (Hodson, 2006; Voinot et al., 2013), and (b) closed-system experiments where biotite was reacted in batch mode with a variety of solutions (Turpault and Trotignon, 1994; Balland et al., 2010). All of the open-system experiments were performed for days to months, allowing the determination of steady-state, far from equilibrium dissolution rates. However, significant changes in both surface area and reacting mineral composition can occur during such open-system experiments, requiring the careful consideration of surface area normalisation (Brantley, 2003; Hodson, 2006). Often, rate data from open-system experiments are normalised to an initial surface area and initial mineral composition, and changes in either of these parameters are not considered. Conversely, closed-system experiments are usually performed over shorter timescales (hours to days) and these allow primarily the characterisation of the initial stages of dissolution. However, rates determined from these shorter, closed-system experiments can be significantly affected by rapidly changing fluid compositions, and rates can be influenced by secondary phase precipitation (Oelkers et al., 2001; Brantley, 2003). To overcome this lacuna, we have performed both mixed-flow (open-system) and batch (closed-system) experiments with the same biotite, at equivalent conditions and derived, compared, and contrasted dissolution rates from both systems.

Finally, most past studies only focussed on the abiotic biotite dissolution. In natural settings, however, biotite is a prime source of nutrients (K in particular) and thus biotic processes may play an important role in element release. Several recent studies have demonstrated that microorganisms influence phyllosilicate weathering through a combination of physical and chemical alteration, or 'bio-fracking' (Balogh-Brunstad et al., 2008; Bonneville et al., 2009, 2011; Hopf et al., 2009; Balland et al., 2010; Saccone et al., 2012; Gazzè et al., 2012, 2013). One bio-mediated mechanism is changing the chemical composition of the local environment, i.e., localised acidification (Balogh-Brunstad et al., 2008; Bonneville et al., 2011). Such acidification is the result of microbial/fungal respiration and the release of organic acids in the near environments of living microorganisms (Bonneville et al., 2011; Gazzè et al., 2013). The effects of which have been considered in several studies attempting to quantify the effect of organic ligands (low molecular weight organic acids and siderophores) on biotite dissolution (e.g., Drever and Stillings, 1997; Balland et al., 2010; Voinot et al., 2013). The results suggest a catalysing effect of organic ligands on phyllosilicate weathering (i.e., a doubling of the dissolution rates) in the presence of high concentrations of organic ligands (i.e., $>10^{-3}$ M, Golubev et al., 2006; Balland et al., 2010). However, the effect of organic ligands on mineral dissolution at the low concentration levels typically found in soils (10^{-5} to 10^{-6} M, Jones, 1998; Ullman and Welch, 2002), and known to be secreted by microorganisms ($<10^{-3}$ M, Adeyemi and Gadd, 2005) is unclear.

Furthermore, only a few data sets testing the effects of organic ligands on biotite dissolution exist (Balland et al., 2010; Voinot et al., 2013). Balland et al. (2010) describe the release of Fe from biotite and phlogopite in closed-system experiments from approximately pH 2–7, both abiotically and in the presence of relatively high concentrations (10^{-2} and 10^{-3} M) of gluconic acid and citric acid. However, data on the release of other elements is absent. Voinot et al. (2013) present a dissolution rate enhancement of almost an order of magnitude in the presence of citric acid at pH 3 and 4.5, compared to open-system abiotic biotite dissolution experiments. Here, we have reacted biotite with three organic ligands (citric acid, oxalic acid, and the siderophore desferrioxamine B, DFOB) and assessed their influence on the release of elements (Al, Fe, Mg and Si) and biotite dissolution rates between pH 2 and 6.

In summary, the objectives of this study were to quantify the control of (a) bulk mineral chemistry, (b) grain size and geometry, (c) experimental approach, and (d) aqueous fluid composition, including organic ligands, on biotite dissolution rates. Experimental results were used to illustrate the effect of the presence of microorganisms both in laboratory and field settings, aiding our understanding of natural soil based processes.

2. MATERIALS AND METHODS

2.1. Mineral samples

The chemical composition and stoichiometric formulas of the two biotite samples (Grasåsen and Moen, both Norway) used in this study have previously been described (Moen – Bonneville et al., 2009; Grasåsen – Bray et al., 2014) and are summarised in Table S1. Each sample was crushed separately using a jaw crusher, pestle and mortar, ball mill, and agate disk mill, removing inclusions throughout. The crushed biotite samples were subsequently sieved to obtain the 75–150 μm (Moen), and 25–53, 53–180, and 180–500 μm (Grasåsen) size fractions. Each size fraction was then washed ultrasonically 10 times in 18.2 MΩ water, separated by gravitational settling, and dried at 40 °C for 48 h.

Post washing, an aliquot of each size fraction was imaged using a field emission gun scanning electron microscope (FEG-SEM, FEI Quanta 650 equipped with an Oxford X-Max silicon drift detector, SDD, operated at 20 kV) on a stage set at a 45° angle to determine grain geometries. From these measurements the geometric specific surface area (SSA_{geo}, $m^{-2}\,g^{-1}$), and the average edge (SA_{edge} %) and basal plane (SA_{basal} %) proportions of each size fraction were determined (Supplementary Information). The specific surface area (SSA_{BET}, $m^{-2}\,g^{-1}$) of each size fraction, and of the post reaction solids, was measured via a 9 point N_2 adsorption isotherm between 0.05 and 0.25 p/p_o (equilibrium pressure/saturation pressure) at 77 K using a Micromeritics Gemini V analyser. Samples were purged with N_2 for 20 h before analysis and the surface area was calculated using the BET method (Brunauer et al., 1938) based on an assumed cross section of adsorbed N_2 of 0.162 nm^2. Replicate measurements of 76 sub-samples of the 53–180 μm size fraction (measured at the start of each closed-system Grasåsen biotite experiment) yielded a relative standard deviation (RSD) of 4.6%. The SSA_{BET}, SSA_{geo}, SA_{edge}, and SA_{basal} of each size fraction are given in Table 1, with the details of calculation of grain geometries presented in the Supplementary Information. Images of the post washing, pre-reaction biotite grains are shown in Fig. S1.

2.2. Dissolution experiments

2.2.1. Closed-system experiments

In total, 91 closed-system experiments were conducted in 1 L high density polyethylene bottles (HDPE, Nalgene), with each experimental condition for the Grasåsen biotite performed in triplicate. The bottles were placed in a 25 ± 1 °C incubator for up to 12 h where they were constantly shaken at 140 rpm, each bottle was also vigorously shaken manually at least once every hour. For each experiment, 1–2 g of biotite was added to 1 L of experimental fluid. Two types of experimental fluids were prepared: (i) one set of experiments (using the Moen biotite) was performed with aqueous 0.003 moles kg^{-1} $CaCl_2$ fluids (ionic strength = 0.01 M, AnalaR NORMAPUR, VWR), with the pH adjusted to between 2 and 6 using HCl/NaOH (Aristar/AnalaR NORMAPUR, VWR); (ii) a second, larger set of experiments (using the Grasåsen biotite) was performed with fluids that were buffered at a selected pH from 2

Table 1
Specific and relative surface area of biotite powder size fractions.

	25–53 μm		Grasåsen				Moen	
			53–180 μm		180–500 μm		75–150 μm	
SSA_{BET} ($m^2\,g^{-1}$)	3.25 [a]	±0.05	0.92 [b]	±0.09	0.64 [c]	±0.07	2.63 [d]	±0.08
SSA_{geo} ($m^2\,g^{-1}$)	0.40		0.19		0.18		0.24	
SA_{edge}	11.6% [e]	±12.4%	7.0% [f]	±10.6%	2.2% [g]	±2.3%	4.1% [h]	±5.9%
SA_{basal}	88.4% [e]	±12.4%	93.0% [f]	±10.6%	97.8% [g]	±2.3%	95.9% [h]	±5.9%
Roughness factor (SSA_{BET}/SSA_{geo})	8.12		4.86		3.53		11.16	
$SSA_{BET\ post}$ (Δ%)			pH 2.56	+0.6% [i]				
			pH 5.95	−2.3% [j]				
			pH 5.98	−11.8% [k]				

[a] $n = 3$; [b] $n = 76$; [c] $n = 3$; [d] $n = 1$; [e] $n = 50$; [f] $n = 50$; [g] $n = 25$; [h] $n = 18$; [i] Post reaction samples from ligand free closed-system experiments at pH ~2.5 (CS-G01–03); [j] Post reaction samples from ligand free closed-system experiments at pH ~6 (CS-G19–21); [k] Post reaction samples from DFOB closed-system experiments at pH ~6 (CS-G49–51).

to 6 with potassium hydrogen phthalate (KHP, $C_8H_5KO_4$, CertiFied AR, Fisher). KHP was used as a background electrolyte to fix the ionic strength and to buffer pH, because initial experiments with $CaCl_2$ showed a strong pH buffering capacity of the Grasåsen biotite due to a $CaCO_3$ impurity of approximately 3.7 wt.%, as previously described (Bray et al., 2014). Experiments were also conducted using both types of experimental fluids to which 500 μmoles kg^{-1} of either citric acid ($C_6H_8O_7$), DFOB ($C_{25}H_{48}N_6O_8$), or oxalic acid ($C_2H_2O_4$) were added. Details for all experimental conditions are given in Table 2. The temporal pH evolution in each experimental condition (with each biotite and experimental fluid matrix, with or without organic acids added) was monitored in additional experiments that were not used for dissolution measurements. In these experiments a semi-micro, epoxy pH electrode (VWR 662-1767), calibrated using NIST traceable buffer solutions of pH 4.01, 6.99, and 9.99 (Fisher Scientific UK) at 25 °C, and connected to an Orion Dual Star pH meter (Thermo Scientific), was constantly immersed in the experimental fluids and the pH was logged every 5 min during the 12 h experiment. Furthermore, in all dissolution experiments the initial, intermediate, and final pH was measured. The maximum pH variance in each experiment was ±0.08 pH units (based on average of 2σ of pH for each experiment, 95% confidence).

During each 12 h closed-system experiment, and with decreasing frequency as each experiment progressed, up to 20 sample aliquots containing 5 mL of a mixture of experimental fluid and biotite particles were removed using a 5 mL syringe from the 1 L containers. Removed samples were immediately filtered through 0.2 μm polyethersulfone filters (Sartorius) and quenched in 3% HNO_3 (Aristar, VWR), HCl (Aristar, VWR) or NaOH (AnalaR NORMAPUR, VWR) depending on subsequent analysis. At the end of each 12 h experiment, the remaining fluids were separated from the reacted biotite by centrifugation. All fluids were analysed as described below, and the reacted biotite powders were dried for subsequent imaging and analysis. Fluid samples were analysed for Al, Fe, Mg, and Si by inductively coupled plasma mass spectrometry (ICP-MS, Agilent 7500ce with integrated auto-sampler, analytical error 6.3%). The detection limit for Al, Fe, Mg, and Si, determined from calibration curves, was 0.8, 0.6, 5.3, and 4.7 μg kg^{-1}, respectively. The average analytical uncertainty, measured against two certified reference materials for Al, Fe, and Mg (SLRS-5 CRM, National Research Council Canada; NWTM-27.3, LGC Standards), and an in-house standard for Si, was determined to be 5.7%, 6.7%, 1.1%, and 7.9%, respectively. To cross-check our data quality, Mg was also analysed by atomic absorption spectroscopy (AAS, Analytik Jena Contraa 700, maximum analytical uncertainty of 2.8%). The detection limit for Mg by AAS was 2.6 μg kg^{-1} with a maximum analytical uncertainty of 7.8%.

2.2.2. Open-system experiments

Both the Moen and Grasåsen biotite samples were reacted in open-system experiments with aqueous fluids of pH 2–4 and at constant ionic strengths. Two distinct mixed-flow reactor systems were used.

The Moen biotite was reacted with an aqueous $CaCl_2$ solution of 0.01 M ionic strength at pH 3.3 in a 300 mL titanium Parr™ mixed-flow reactor at controlled temperature, pressure, and under constant stirring and continuous pH monitoring following the approach described in Wolff-Boenisch et al. (2004). Briefly, approximately 6 g of the 75–150 μm biotite size fraction was reacted in a stirred (400 rpm) 300 mL mixed-flow reactor, for up to 260 h with a fluid continuously pumped through the reactor with a high performance liquid chromatography (HPLC) pump at flow rates from 1.2 to 2.2 g/min. At the system outlet, the fluid passed through a 2 μm titanium filter to prevent the escape of solids. The outflow fluids were further filtered using 0.2 μm polyvinylidene fluoride (PDVF) Whatman™ filters and collected in acid washed HDPE sample bottles, pre-acidified with HNO_3 (Aristar, VWR). The solids were recovered at the end of each experiment by centrifugation and dried for further analyses.

The Grasåsen biotite was reacted with fluids at pH from 2 to 4 and at an ionic strength of 0.01 M, fixed using HCl, NaCl, or KHP, with the KHP used as a pH buffer and ionic strength matrix (see above). Experiments were conducted in a water bath at a constant temperature of 25 ± 1 °C in 35 mL Teflon mixed-flow reactors that were continuously stirred with floating Teflon magnetic stirring bars. Each reactor consisted of identical base and head compartments (Köhler et al., 2005; Chaïrat et al., 2007; Flaathen et al., 2010; Declercq et al., 2013) and the added biotite powder (1–1.5 g) was kept in the reactor using 0.45 μm GN-6 Metricel MCE membrane filters. During the experiments (up to approximately 800 h) fluids were pumped through the reactors via a peristaltic pump at rates from 0.1 to 0.6 g/min. Samples were collected in HDPE bottles, pre acidified with 3% analytical grade HNO_3. Fluid pH was measured at the start of each experiment and in each fluid sample taken during the experiments, using a Metrohm 713 pH Meter, calibrated with certified reference buffer solutions of pH 4.005, 6.866, and 9.183 (CertiPUR, Merck) at 25 °C. pH measurement precision was 0.02 pH units. Dissolved silica concentrations in the outlet fluids were determined using the colorimetric molybdate blue method (Bran & Luebbe AutoAnalyzer 3, maximum analytical uncertainty ±3.5%). Concentrations of Fe, Mg, and Al were determined by AAS using a Perkin Elmer 5100 PC spectrometer with maximum analytical uncertainty of 2.8%. The details of the open-system experiments are listed in Table 3.

2.3. Experimental fluid modelling

The speciation of organic ligands and dissolved elements in the experimental fluids and the saturation state of the fluids with respect to potential secondary phases were calculated using the PHREEQC3 computer code and the minteq.v4 database (Parkhurst and Appelo, 2013). The results of these calculations were used to interpret the experimental results as discussed below.

Table 2
Details of the closed-system experiments, fitting parameters, and analytical rates.

	Exp.	Matrix [a]	SIZE fraction		Surface area	Fitting parameters								Biotite dissolution rate							
						Al		Fe		Mg		Si		$\log r_{Al}$	$\log r_{Fe}$	$\log r_{Mg}$	$\log r_{Si}$	$\log r_{Al}$	$\log r_{Fe}$	$\log r_{Mg}$	$\log r_{Si}$
			μm	pH	$m^2\ L^{-1}$	k' 10^{-7}	q	k' 10^{-7}	q	k' 10^{-7}	q	k' 10^{-7}	q	$t = 1$ s	$t = 1$ s	$t = 1$ s	$t = 1$ s	$t = 12$ h	$t = 12$ h	$t = 12$ h	$t = 12$ h
Grasåsen	CS-G01–03	KHP	53–180	2.56	1.95	7.19	0.25	6.25	0.28	6.56	0.26	3.08	0.25	−6.74	−6.76	−6.77	−7.12	−10.21	−10.11	−11.62	−10.61
	CS-G04–06		53–180	3.21	2.00	7.51	0.20	5.93	0.24	7.05	0.22	3.22	0.20	−6.81	−6.84	−6.81	−7.19	−10.50	−10.35	−11.92	−10.89
	CS-G07–09		53–180	4.16	1.98	2.91	0.25	1.41	0.33	3.18	0.27	2.60	0.19	−7.13	−7.33	−7.17	−7.30	−10.60	−10.44	−11.27	−11.03
	CS-G10–12		25–53	4.47	6.73	11.00	0.15	9.72	0.13	12.94	0.16	4.67	0.17	−6.78	−6.88	−6.68	−7.11	−10.73	−10.90	−12.48	−10.98
	CS-G13–15		180–500	4.10	1.32	1.70	0.30	0.29	0.48	3.35	0.25	1.24	0.23	−7.29	−7.86	−7.08	−7.55	−10.54	−10.28	−11.71	−11.13
	CS-G16–18		53–180	5.18	2.02	0.80	0.33	0.30	0.41	1.15	0.34	1.43	0.22	−7.58	−7.91	−7.40	−7.51	−10.66	−10.66	−10.97	−11.15
	CS-G19–21		53–180	5.95	1.89	1.81	0.11	0.17	0.28	2.02	0.23	1.61	0.12	−7.69	−8.31	−7.34	−7.71	−11.81	−11.66	−11.86	−11.78
	CS-G22–24	KHP + Citric acid	53–180	2.60	1.97	7.02	0.25	8.23	0.25	5.53	0.27	3.93	0.21	−6.75	−6.68	−6.83	−7.07	−10.22	−10.14	−11.52	−10.71
	CS-G25–27		53–180	3.07	1.85	4.96	0.26	3.26	0.31	3.85	0.29	3.27	0.22	−6.88	−6.99	−6.95	−7.15	−10.30	−10.17	−11.37	−10.79
	CS-G28–30		53–180	3.95	1.96	6.26	0.21	4.36	0.26	4.89	0.24	3.24	0.21	−6.89	−6.94	−6.93	−7.17	−10.57	−10.36	−11.75	−10.85
	CS-G31–33		53–180	4.96	1.85	1.93	0.29	0.89	0.39	1.87	0.32	1.16	0.27	−7.25	−7.46	−7.22	−7.50	−10.55	−10.29	−11.15	−10.88
	CS-G34–36		53–180	5.70	1.87	0.54	0.38	0.14	0.53	0.79	0.38	0.11	0.47	−7.69	−8.12	−7.53	−8.30	−10.58	−10.31	−10.74	−10.76
	CS-G37–39	KHP + DFOB	53–180	2.52	1.73	8.34	0.26	10.79	0.24	7.66	0.25	4.26	0.21	−6.67	−6.58	−6.72	−7.05	−10.12	−10.10	−11.71	−10.73
	CS-G40–42		53–180	3.16	1.79	1.65	0.38	1.68	0.40	1.65	0.38	0.70	0.35	−7.21	−7.17	−7.21	−7.61	−10.09	−9.95	−10.74	−10.65
	CS-G43–45		53–180	4.18	1.81	1.58	0.32	1.57	0.35	1.45	0.33	0.59	0.29	−7.30	−7.26	−7.32	−7.76	−10.46	−10.27	−11.04	−11.04
	CS-G46–48		53–180	5.21	1.85	0.54	0.41	0.47	0.46	1.02	0.36	0.08	0.48	−7.66	−7.67	−7.43	−8.42	−10.41	−10.20	−10.83	−10.82
	CS-G49–51		53–180	5.98	1.85	0.30	0.43	0.18	0.52	0.81	0.36	0.16	0.40	−7.89	−8.04	−7.53	−8.19	−10.54	−10.26	−10.85	−10.97
	CS-G52–54	KHP + Oxalic acid	53–180	2.50	1.90	11.08	0.23	12.07	0.23	7.89	0.24	3.14	0.24	−6.59	−6.56	−6.71	−7.13	−10.16	−10.12	−11.72	−10.66
	CS-G55–57		53–180	3.06	1.80	10.19	0.22	10.74	0.23	7.49	0.23	4.13	0.19	−6.65	−6.61	−6.75	−7.10	−10.27	−10.18	−11.80	−10.86
	CS-G58–60		53–180	3.94	1.88	10.71	0.17	7.07	0.23	5.94	0.22	1.11	0.25	−6.73	−6.79	−6.88	−7.55	−10.57	−10.36	−11.92	−11.01
	CS-G61–63		53–180	4.99	1.80	2.97	0.25	1.42	0.34	1.83	0.31	0.87	0.28	−7.13	−7.32	−7.24	−7.62	−10.61	−10.39	−11.20	−10.97
	CS-G64–66		53–180	5.74	1.87	0.26	0.43	0.51	0.37	0.21	0.48	0.51	0.27	−7.95	−7.72	−8.00	−7.87	−10.59	−10.65	−10.02	−11.27

	Exp.	Matrix	Size fraction		Surface area	Fitting parameters								Biotite dissolution rate							
						Al		Fe		Mg		Si [b]		$\log R_{Al}$	$\log R_{Fe}$	$\log R_{Mg}$	$\log R_{Si}$	$\log R_{Al}$	$\log R_{Fe}$	$\log R_{Mg}$	$\log R_{Si}$
			μm	pH	$m^2\ L^{-1}$	k' 10^{-7}	q	k' 10^{-7}	q	k' 10^{-7}	q	k' 10^{-7}	q	$t = 1$ s	$t = 1$ s	$t = 1$ s	$t = 1$ s	$t = 12$ h	$t = 12$ h	$t = 12$ h	$t = 12$ h
Moen	CS-M01	$CaCl_2$	75–150	2.00	2.47	10.74	0.23	19.75	0.16	25.62	0.22	–	–	−6.60	−6.50	−6.25	–	−10.16	−10.40	−9.86	–
	CS-M02		75–150	4.00	2.44	6.63	0.13	11.82	0.09	17.64	0.12	–	–	−7.06	−6.96	−6.68	–	−11.10	−11.16	−10.77	–
	CS-M03		75–150	6.00	2.42	–	–	–	–	17.09	0.07	–	–	–	–	−6.92	–	–	–	−11.24	–
	CS-M04	$CaCl_2$ + Citric acid	75–150	2.00	2.44	26.02	0.11	6.69	0.23	14.96	0.22	–	–	−6.55	−6.81	−6.48	–	−10.68	−10.38	−10.08	–
	CS-M05		75–150	4.00	2.45	5.76	0.17	9.59	0.16	17.00	0.15	–	–	−7.00	−6.82	−6.61	–	−10.82	−10.73	−10.57	–
	CS-M06		75–150	6.00	2.44	2.51	0.16	13.56	0.06	12.29	0.12	–	–	−7.40	−7.07	−6.82	–	−11.30	−11.42	−10.89	–
	CS-M07	$CaCl_2$ + DFOB	75–150	2.00	2.48	2.19	0.38	4.32	0.31	8.51	0.31	–	–	−7.08	−6.87	−6.58	–	−9.95	−10.08	−9.77	–
	CS-M08		75–150	4.00	2.42	6.95	0.20	10.86	0.17	52.78	0.11	–	–	−6.87	−6.73	−6.24	–	−10.59	−10.57	−10.37	–
	CS-M09		75–150	6.00	2.25	0.21	0.38	9.28	0.12	4.28	0.21	–	–	−8.10	−6.96	−7.05	–	−10.97	−11.05	−10.72	–

[a] The matrix of the experimental fluid was at an ionic strength of 0.01 moles L^{-1}, fixed using either potassium hydrogen phthalate (KHP) or $CaCl_2$. The concentration of citric acid, DFOB, and oxalic acid, when present in the closed system experiments, was 0.0005 moles L^{-1}.

[b] Released silica concentrations were not measured in the closed-system Moen biotite experiments.

3. RESULTS

3.1. Closed-system experiments

The measured aqueous element concentrations ($c_{i,t}$) released as a function of time in all closed-system experiments are provided in Table S2. To quantify the rates of biotite dissolution the number of moles of each element, i, in the fluid phase at time t ($m_{i,t}$), normalised to biotite stoichiometry (Table S1) and the surface area present in the reactor (from the initial BET specific surface area, s) (Table 1), is defined as $m'_{i,t}$, and calculated through:

$$m'_{i,t} = \frac{m_{i,t}}{s \cdot M \cdot n_i} = \frac{c_{i,t} \cdot V_t}{s \cdot M \cdot n_i} \quad (1)$$

where $c_{i,t}$ (moles kg^{-1}) designates the measured fluid concentration of element i at time t, V_t refers to the mass (kg) of aqueous fluid in the reactor at time t, s represents the initial specific surface area of biotite powder (m^2 g^{-1}, SSA_{BET}), M the mass of biotite powder (g), and n_i the stoichiometry of the ith element in the biotite formula. Resulting values of $m'_{i,t}$ are shown in Figs. 1 and 2.

Element release during the closed-system dissolution experiments was highly pH dependent and, in part, non-stoichiometric. In organic ligand-free experiments at pH 2.5, when normalised to the dissolving biotite stoichiometry, the release of Mg, Fe, and Al was largely stoichiometric with respect to one another, while Si release was 2.5–3 times lower (Fig. 1A). With increasing pH the released element concentrations decrease (Fig. 1B) with the final concentrations (after 12 h) at pH ~6 being ~1 order of magnitude lower than those at pH 2.5 (Fig. 1C). Increased pH also results in more pronounced non-stoichiometric release, with preferential Mg release over other elements at pH > 4 (Fig. 1C).

In experiments at approximately pH 4, where the same Graså sen biotite but different particle size fractions were used (Tables 1 and 2), the element release profiles, plotted as biotite stoichiometry and surface area normalised values, show a marked increase in element concentration with decreasing particle size (Fig. 1D, Fig. S2). For aluminium, magnesium and silica in all cases, after 12 h, the smallest biotite size fraction (25–53 μm) released Al, Mg and Si between 0.5 and 2 times faster than the 53–180 and 180–500 μm size fractions respectively (Fig. 1D and Fig. S2A, C and D). In contrast, iron release (Fig. S2B) appeared independent of particle size. One possible explanation for this is the precipitation of the dissolved iron in secondary phases. The fluids at the end of the organic ligand-free experiments (12 h) for each size fraction at pH 4 (experiments CS-G07 to G15, Table 2) were calculated to be supersaturated with respect to Fe-phases (ferrihydrite, goethite and hematite; Table S3). However, FEG-SEM imaging of the reacted biotite solids, even at the highest resolution (~20 to 50 nm particles), did not reveal any secondary phases. Such phases were only observed on particles retrieved from the organic ligand-free closed-system experiments at pH 6 (see CS-G19–21, Table 2, Fig. S1D) where the solubility of secondary Fe and Al phases is minimal. Precipitation of such secondary phases could result in

Table 3
Details of the open-system experiments and calculated dissolution rates.

Exp.	Matrix	Additive		pH	m	Flow	c_{Al}	c_{Fe}	c_{Mg}	c_{Si}	$\log r_{Al}$	$\log r_{Fe}$	$\log r_{Mg}$	$\log r_{Si}$
			μmol kg^{-1}		g	g min^{-1}	mol kg^{-1} 10^{-5}				moles m^{-2} s^{-1}			
OS-G01	HCl	–	–	2	1.03	0.18	13.03	10.96	13.31	17.81	−9.50	−9.49	−9.53	−9.69
OS-G02	HCl	Oxalic acid	500	2	1.08	0.21	14.37	11.77	15.12	20.52	−9.41	−9.42	−9.45	−9.62
OS-G03	HCl	Citric acid	500	2	1.01	0.21	9.56	7.08	8.85	12.49	−9.60	−9.65	−9.67	−9.83
OS-G04	NaCl	Oxalic acid	500	3.3	1.05	0.21	1.03	1.79	2.04	3.26	−10.55	−10.24	−10.30	−10.39
OS-G05	NaCl	–	–	3.1	1.04	0.17	1.46	2.33	2.44	2.84	−10.48	−10.20	−10.30	−10.53
OS-G06	NaCl	–	–	4.4	1.07	0.17	–	–	–	0.53	–	–	–	−11.28
OS-G07	NaCl	Citric acid	500	3.1	1.03	0.18	9.28	5.73	7.30	8.12	−9.64	−9.78	−9.79	−10.04
OS-G08	NaCl	–	–	3.1	1.11	0.19	2.48	3.09	3.64	5.03	−10.22	−10.05	−10.10	−10.25
OS-G09	NaCl	–	–	3.1	1.11	0.21	1.67	2.97	3.40	4.59	−10.38	−10.06	−10.11	−10.28
OS-G10	KHP	–	–	4.1	1.49	0.12	0.30	0.55	0.47	0.48	−11.50	−11.15	−11.34	−11.62
OS-G11	KHP	Citric acid	500	3.9	1.49	0.12	0.53	0.73	0.71	0.74	−11.26	−11.04	−11.17	−11.45
OS-G12	KHP	–	–	4.1	1.54	0.11	0.35	0.60	0.53	0.59	−11.48	−11.17	−11.34	−11.59
OS-G13	KHP	Oxalic acid	500	3.90	1.54	0.10	1.06	1.07	1.17	1.12	−11.01	−10.93	−11.01	−11.32
OS-M1	$CaCl_2$	–	–	3.4	6.04	1.16	1.12	0.15	1.08	2.30	−11.04	−11.95	−10.77	−11.00
OS-M2	$CaCl_2$	Citric acid	500	3.3	6.04	1.89	3.37	0.44	3.10	3.61	−10.59	−11.27	−10.10	−10.35
OS-M3	$CaCl_2$	Citric acid	500	3.00	6.04	1.87	5.08	0.19	5.49	4.15	−10.53	−11.64	−9.85	−10.18
		DFOB	145											

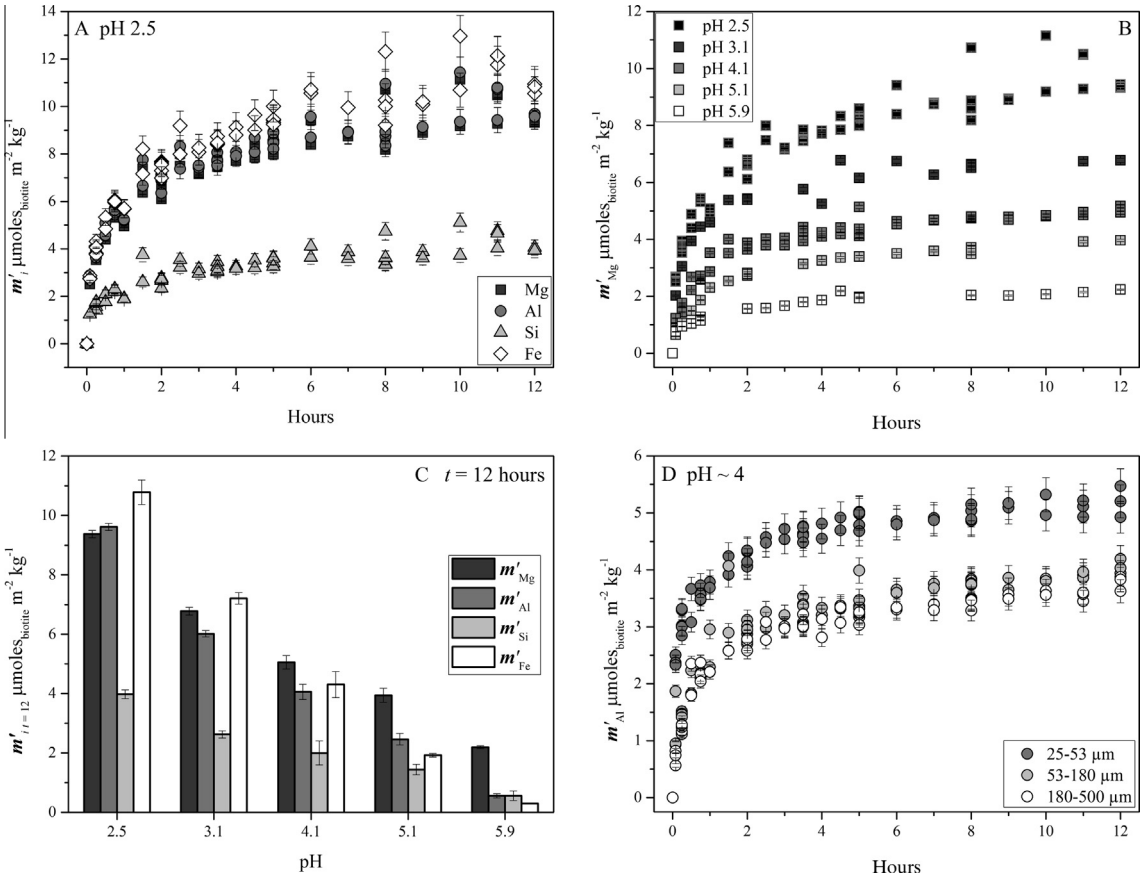

Fig. 1. Element release data from the closed-system ligand-free Grasåsen biotite dissolution experiments (CS-G01–21). (A) Element release at pH 2.5 (CS-G01–03), (B) Mg release at each pH, (C) Element concentration at the end of experimental period of 12 h, and (D) Al release at pH ~4 from the 25–53, 53–180, and 180–500 µm Grasåsen biotite size fractions, experiments CS-G07–15. Error bars in (A), (B), and (D) represent the analytical uncertainty for each element, and (C) 2 standard deviations of the average from triplicate experiments.

changes in the specific surface area of reacted biotite solids. Specific surface area measurements of the reacted biotite solids from the experiments with the greatest release of elements (exp. CS-G01–03, Table 2), and the largest calculated supersaturation with respect to secondary Fe and Al phases (exp. CS-G19–21, Table 2), only revealed specific surface area changes of +0.6% and −2.3%, respectively, which are both within the uncertainty of measurement (9.2%, two relative standard deviations based on 76 replicates of the original material, Table 1).

In experiments with organic ligands present, at low pH (pH 2.5, Fig. 2A), there was no appreciable effect on Si release. However, at pH 3 and above, the presence of organic ligands increases element release relative to ligand-free experiments. This is most evident for Fe and Al (Fig. 2B and C) where, compared to the ligand-free system, the end-experiment Al and Fe concentrations in the presence of all organic acids were between 2 and 6 times higher. A similar pH dependent behaviour is evident for the final Mg concentration ($t = 12$ h) shown in Fig. 2D. These element release profiles are representative of the overall trend of the effect of ligand presence observed for Al, Fe, Mg, and Si at pH values between pH 2.5 and 6. All other element release profiles are presented in Fig. S3.

Evaluating dissolution rates from closed-system experiments is challenging because kinetic calculations must consider the constantly changing fluid composition and the effect of possible saturation controlled back reactions (Oelkers et al., 2001; Brantley, 2003). The release of elements into the fluid during our short-term, 12 h, closed-system experiments followed a trend typical for most closed-system dissolution studies (e.g., Oelkers et al., 2001) where rapid release of elements occurs in the first stage of the reaction followed by a slower, decreasing release with time. The element release profiles can be modelled (Fig. 3A) according to:

$$\boldsymbol{m}'_{i,t} = k' t^{q} \tag{2}$$

where k' designates a rate constant (moles m^{-2} s^{-q}), t refers to time in seconds, and q stands for the exponential decay of the release rate (dimensionless). In Eq. (2), the values of k' and q can be derived through a linear regression of the logarithm of $\boldsymbol{m}'_{i,t}$ and t, where q corresponds to the slope of the regression and $\log k'$, its intercept ($\log t = 0$, $t = 1$ s). The values of k' and q for each experimental condition are listed in Table 2.

The element release profile shown in Fig. 3A is typical for the closed-system dissolution experiments. Such profiles

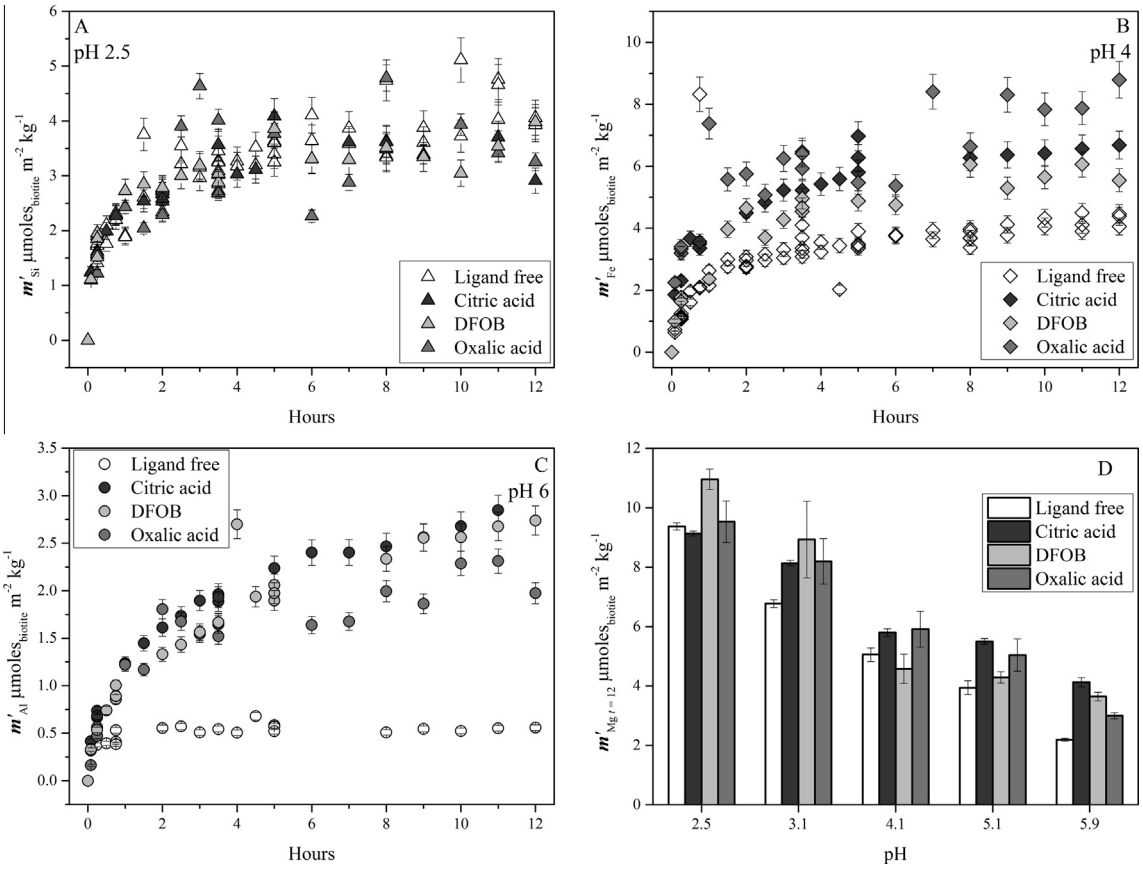

Fig. 2. Element release in closed-system experiments in the presence of organic acids. (A) Time resolved Si release at pH 2.5, (B) time resolved Fe release at pH 4, (C) time resolved Al release at pH 6, and (D) final Mg concentration ($t = 12$ h) as a function of organic acid added. The element release profiles from all the Graså sen closed-system experiments can be seen in Fig. S2. Error bars in (A), (B), and (C) represent the analytical uncertainty for each element, and (D) 2 standard deviations of the average from triplicate experiments.

can be interpreted to stem from (1) the initial rapid release of elements from fine particles or highly reactive sites, and (2) the slowing of rates due to an approach to equilibrium, or (3) a slowing of rates due to the increase of one or more aqueous species that inhibit dissolution (Oelkers and Schott, 2001; Gautelier et al., 2007; Saldi et al., 2007, 2010; Oelkers et al., 2008). Based on these profiles, we determined rates directly from the derivative of the element masses versus time throughout each experiment. The dissolution rate can be calculated analytically from the derivative of Eq. (2):

$$r_{i,t} = \frac{\partial \boldsymbol{m}'_i}{\partial t} = qk't^{(q-1)} \tag{3}$$

where $r_{i,t}$ represents the dissolution rate ($\text{moles}_{\text{biotite}}\ \text{m}^{-2}\ \text{s}^{-1}$) with respect to the ith element at time t. The calculated biotite dissolution rates for each closed-system experiment at $t = 1$ s and $t = 12$ h are shown in Table 2. The results reveal that for all elements the dissolution rates decrease with time, with the rate at 12 h approximately 4 orders of magnitude slower than the initial dissolution rate ($t = 1$ s). The causes of the differences in these rates will be discussed below.

3.2. Open-system experiments

In the organic ligand and ligand-free open-system experiments the element release rates approached a near steady-state after at least 100 h (Fig. 3B). Steady-state was defined by the outlet fluids maintaining a constant concentration of Al, Fe, Mg, and Si, within 5% (analytical and experimental uncertainty) for a minimum of 3 residence times (reactor volume/flow rate). In the case of the Graså sen biotite at pH 2, steady-state was attained after ~125 h. Based on this, the average element concentrations released after 125 h (Table 3) were used to calculate steady-state biotite dissolution rates according to:

$$r_i = \frac{\text{f} \cdot \boldsymbol{c}_i}{\boldsymbol{s} \cdot M \cdot n_i} \tag{4}$$

where r_i denotes the surface area normalised steady-state dissolution rate ($\text{moles}_{\text{biotite}}\ \text{m}^{-2}\ \text{s}^{-1}$), f symbolises the fluid flow rate ($\text{kg}\ \text{s}^{-1}$), $\boldsymbol{c}_i$ signifies the aqueous concentration of the ith element in the outlet fluid ($\text{moles}\ \text{kg}^{-1}$), $\boldsymbol{s}$ stands for the initial specific surface area ($\text{m}^2\ \text{g}^{-1}$, SSA_{BET}) of the mineral powder of mass M (g), and n_i the stoichiometric coefficient of the ith element in the biotite formula (Table S1).

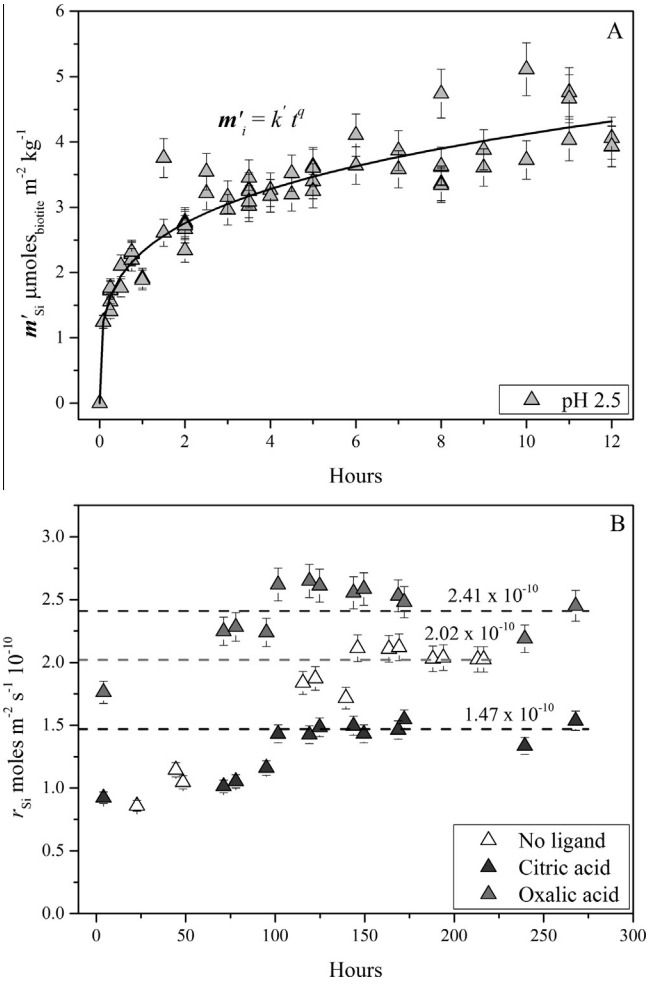

Fig. 3. (A) Experimental data of Si released from biotite during closed-system Grasåsen biotite experiments CS-G01–03, fitted using Eq. (2), to derive the Si release rate during the experiment. (B) Biotite dissolution rates based on Si release from open-system Grasåsen biotite experiments at pH 2. The dashed lines represent calculated steady state dissolution rates. Error bars represent the analytical uncertainty for each element.

The calculated biotite dissolution rates for each open-system experiment are listed in Table 3.

4. DISCUSSION

4.1. pH and organic ligand dependent element release

Consistent with the general trend of multi-oxide silicates (Oelkers and Schott, 2001; Golubev and Pokrovsky, 2006; Schott et al., 2012; Stockmann et al., 2013; Rimstidt, 2014), the Grasåsen and Moen biotite dissolution rates decrease with increasing pH from pH 2–6. The calculated open and closed-system organic ligand-free dissolution rates are plotted as a function of pH in Fig. 4A, along with biotite dissolution rates from the literature. The shaded area in Fig. 4A is used in Fig. 4B–D to highlight the range of kinetic data presented in the literature as a function of pH (Acker and Bricker, 1992; Kalinowski and Schweda, 1996; Malmström et al., 1996; Malmström and Banwart, 1997; Balland et al., 2010; Voinot et al., 2013). The closed-system rates plotted are those calculated for $t = 12$ h, as these are most consistent with open-system and literature data. It is worth noting that, at any given pH, biotite dissolution rates from the literature can range over 1.5 orders of magnitude.

This range of reported rates can be attributed to a number of differences. Firstly, differences in the bulk chemical composition of each biotite sample may result in a range of dissolution rates. The rate data from the literature presented in Fig. 4A span biotite samples from 4 locations: Bancroft, Ontario, Canada (Acker and Bricker, 1992; Voinot et al., 2013); Moen, Norway (Kalinowski and Schweda, 1996; Malmström et al., 1996; Malmström and Banwart, 1997; current study); Raze, Limousin, France (Balland et al., 2010) and Grasåsen, Norway (this study). However, even when a biotite sample was used from the same location some compositional differences remain. For example, in the case of the biotite from Bancroft, Ontario, the reported Mg and Fe present in each sample vary. Acker and Bricker (1992) report moles of Mg and

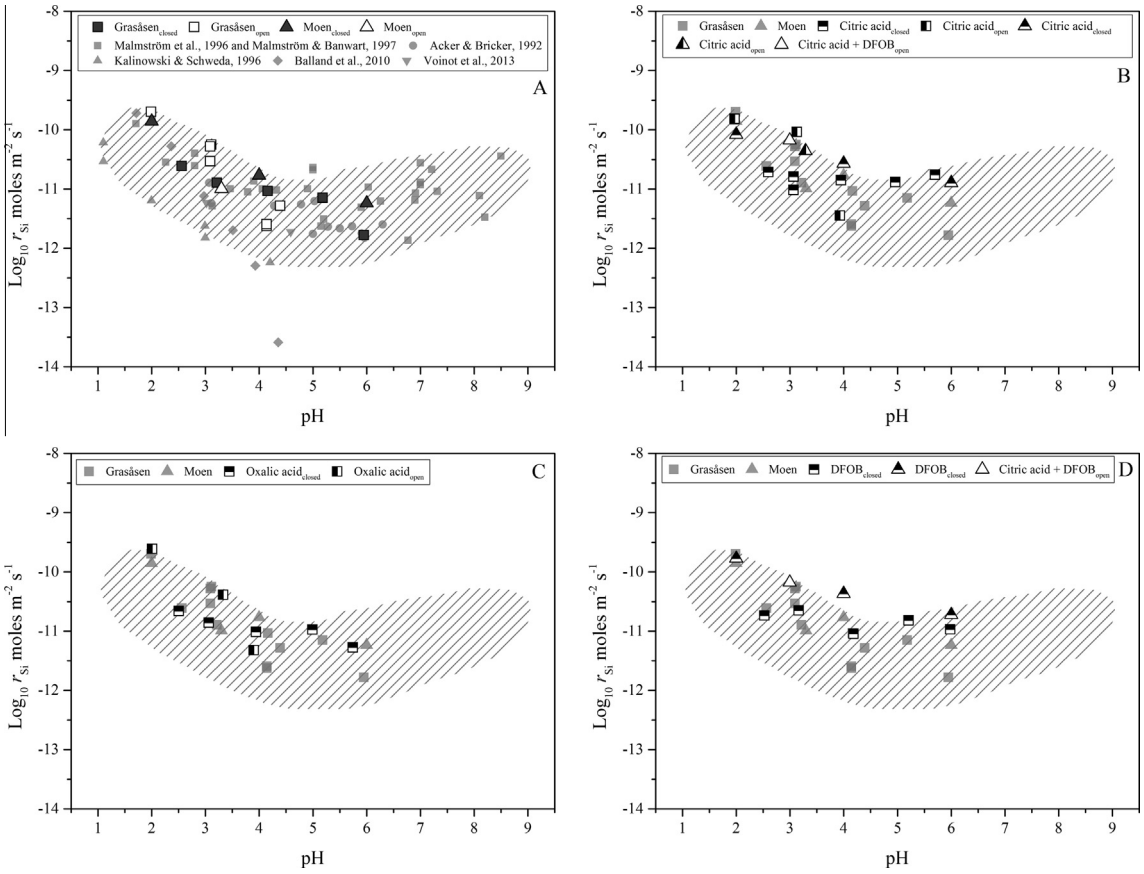

Fig. 4. Biotite dissolution rate data from all closed- and open-system experiments with both Moen and Grasåsen biotite samples together with literature data, plotted against pH. The shaded area guides the eye to show the spread in literature data. (A) Ligand-free, (B) citric acid (incl. citric acid + DFOB), (C) oxalic acid, and (D) DFOB (incl. citric acid + DFOB). The grey symbols in (B), (C), and (D) represent the ligand-free rates determined in this study.

total Fe in one mole of biotite as 1.59 and 1.12 respectively, while in the Bancroft, Ontario biotite used by Voinot et al. (2013) Mg and Fe in the formula are reported as 2.06 and 0.73 moles respectively. Secondly, the anisotropic nature of biotite has previously been described (Turpault and Trotignon, 1994; Hodson, 2006), with differences in grain size, surface area and geometries of the reacting biotite all likely influencing the measured dissolution rates. Thirdly, different experimental approaches, including experiment duration, may also influence dissolution kinetics. For example, for illite, Köhler et al. (2005) reported decreasing dissolution rates with time during flow-through experiments, and attributed these to the changes in clay morphology and a decrease in the number of reactive edge sites. For biotite, the duration of flow-through biotite dissolution experiments in the literature (Fig. 4A) ranges from ~300 (Acker and Bricker, 1992) to 3000 h (Kalinowski and Schweda, 1996). Finally, variations in the chemical composition of the experimental fluids can influence dissolution rates, particularly in closed-system experiments where fluids may become supersaturated with respect to secondary phases.

To evaluate how these various parameters have affected the dissolution rates of the Grasåsen and Moen biotite in the current study, the dissolution rates are described as a function of pH using an empirical rate law for acid promoted dissolution (e.g., Lasaga, 1998):

$$r_i = k_{\mathrm{H},i} a_{\mathrm{H}^+}^{x_i} \quad (5)$$

where r_i again refers to the specific dissolution rate of biotite based on the ith element, $k_{\mathrm{H},i}$, corresponds to a rate constant, and x refers to a reaction order with respect to proton activity, a_{H^+}.

Using Eq. (5), the rate constants and reaction orders derived from the ligand-free experiments for both the Grasåsen and Moen biotite samples were determined by linear-least-square regression of $\log r_i$ against pH (Table 4; Fig. 4A). Results are comparable with the rate constants and reaction orders previously reported for biotite (Acker and Bricker, 1992; Kalinowski and Schweda, 1996; Malmström and Banwart, 1997).

The data derived from the biotite dissolution experiments performed in the presence of citric acid, oxalic acid, and DFOB (Fig. 4B–D) generally lie within the shaded region of the ligand-free biotite dissolution rates shown in Fig. 4A. At low pH (<4), biotite dissolution rates in the presence of citric acid, oxalic acid, and DFOB were within the range of the organic ligand-free data from this study, and the literature. Above pH 4 a slight enhancement in

Table 4
Apparent rate constants k_H (10^{-9} moles m^{-2} s^{-1}), and reaction orders x, with respect to hydrogen ion activity from the Moen and Grasåsen element release data. SE represents the standard error of the apparent rate constants and reaction orders.

		Grasåsen				Moen			Acker and Bricker [a]	Kalinowski and Schweda [a]	Malmström and Banwart [a]
		Al	Fe	Mg	Si	Al	Fe	Mg	Si	Si	Si
k_H 10^{-9}		1.25	1.83	3.06	0.83	0.58	0.21	0.29	0.10 moles m^{-2} s^{-1}	0.16	0.91
SE limits	Max	3.40	3.96	8.14	1.95	1.84	16.86	1.02			
	Min	0.46	0.84	1.15	0.35	0.19	0.003	0.08			
x		0.48	0.47	0.58	0.48	0.49	0.48	0.31	0.30	0.62	0.51
SE		0.11	0.09	0.11	0.10	0.15	0.59	0.13			

[a] Recalculated from Acker and Bricker (1992), Kalinowski and Schweda (1996), and Malmström and Banwart (1997) into rate units of moles m^{-2} s^{-1}, based on a biotite stoichiometric formula normalised to $O_{10}(OH)_2$.

dissolution rate in the presence of all organic ligands could be observed compared to the ligand-free data. However, the ligand dissolution rates are within the range of abiotic biotite dissolution rates reported previously, and in this study (Fig. 4B–D). In comparison, Balland et al. (2010) conducted biotite dissolution experiments in the presence of citric and gluconic acid at ligand concentrations between 10^{-3} and 10^{-2} M. Compared to the data in the current study, Balland et al. (2010) reported an enhanced ligand promoted release rate for Fe, which was up to 2 orders of magnitude faster than their corresponding ligand-free rates. Similarly, Voinot et al. (2013) reported an order of magnitude enhancement in biotite dissolution rates in the presence of citric acid, but they saw no enhancement in the presence of the siderophore DFAM-B.

In the current study, the minor increase of element release from biotite in the presence of organic ligands may be explained by: (1) the relatively low, but more realistic, concentrations of organic ligands used in the experimental fluids, and (2) that biotite dissolution rates have been computed from Si release rather than the release of other aqueous metals.

The effect of organic ligand concentrations on rates is not easy to compare. We used concentrations of citric and oxalic acid of 500 μM each, while DFOB was 500 μM and 145 μM in the closed- and open-system experiments, respectively. These values were chosen to be consistent with organic ligand production values reported for soil-dwelling microorganisms in the literature (Lapeyrie et al., 1987; Lapeyrie, 1988; Adeyemi and Gadd, 2005). However, comparing our data with previous biotite studies where organic ligands were reported to enhance dissolution, revealed that the concentration of citric acid used in the current study was between 2 and 20 times lower than the concentration used by Balland et al. (2010), while the citric acid concentration used by Voinot et al. (2013) was not reported.

Golubev et al. (2006) showed that a system requires a minimum concentration of organic ligands ($\geqslant 10^{-3}$ M) that is between 2 and 7 times higher than the value used here, before an appreciable ligand promoting dissolution effect (i.e., a doubling of dissolution rate) is measurable. Such a critical ligand concentration was also observed in dissolution studies of basaltic glass, where Oelkers and Gislason (2001) found a 2-fold increase in basaltic glass dissolution rates by adding 1000 μM oxalic acid to a pH 3 solution, whereas Wolff-Boenisch et al. (2011) did not find any change in dissolution rates of the same basaltic glass in the presence of 120 μM oxalic acid, at similar pH. The fact that neither Voinot et al. (2013), nor this study, finds any DFOB effect on the Si release rates may well be explained by the similarly low concentrations used in both studies.

Differences in rates between our study and literature studies (Fig. 4) may also stem from the fact that we calculated rates based on the temporal evolution of Si concentrations in the experimental fluid. One of the reasons for the reported effect of citric acid on biotite dissolution rates in the study of Balland et al. (2010) is likely due to their use of the dissolved Fe concentrations, a metal to which citrate has a strong affinity, for their rate calculations. This is because in the absence of organic ligands at slightly acidic pH the solubility of iron is low and enhanced by low concentrations of citric acid. This effect likely leads to the apparent faster rate reported by Balland et al. (2010). This conclusion is strengthened through speciation and metal complexation calculations (Fig. S4) for (A) phthalic acid, (B) citric acid, (C) oxalic acid and (D) DFOB as a function of pH. These plots were calculated from the acid dissociation and stability constants of each ligand (Table S4), the concentrations of Al, Fe and Mg at the end of the pH 2.5 closed system experiments (12 h, Table S2) and using the PHREEQC 3 computer code (Parkhurst and Appelo, 2013). Above pH 2–3 in the presence of citric acid (Fig. S4B), the majority of Fe and Al in the fluid forms citrate complexes. Conversely, Mg–citrate complexes do not become dominant until above pH 6. This poor affinity for the formation of Mg-organic ligand complexes is also reflected in the oxalic acid and DFOB speciation. At pH 1, Fe–oxalate and Fe–DFOB complexes are the dominant form of dissolved Fe, while Al-oxalate, Al-DFOB complexes dominate above pH 2.5 and 2 respectively (Fig.S4C and S4D). We used the same code to calculate the saturation state of the experimental fluids with respect to potential secondary phases in all experiments (Table S3). Compared to a fluid calculated using NaCl as a background electrolyte, the presence of phthalate (from KHP) has little effect on Al and Fe secondary phase saturation. This is due to the poor affinity of phthalate for metals.

In the organic ligand-free experiment, experimental fluids across the pH range studied are supersaturated with respect to iron phases (ferrihydrite, goethite, and hematite), and supersaturated with respect to the Al phase gibbsite at pH > 5. However, the calculated saturation indices for Fe and Al phases are reduced in the experimental fluids with citric acid, oxalic acid and DFOB (Table S3). At least one Fe phase is supersaturated at all pH in the presence of citric acid, and above pH 5 in the presence of oxalic acid. However, Fe phases are undersaturated at all pH in the presence of DFOB, highlighting the powerful chelating ability of the siderophore. Apart from at approximately pH 6 in the presence of oxalic acid, Al phases are all undersaturated in the presence of the organic ligands. The calculated positive saturation values in some near neutral experiments, with respect to secondary iron and aluminium phases, could be due to the presence of nanoparticulate or colloidal iron and aluminium. Particles less than 200 nm in size could have passed through the 0.2 μm filters during sampling, and subsequently been measured as solution based Fe and Al during analysis. However, as the point of zero surface charge for biotite is pH 3 (Bray et al., 2014), and pH 7–9 for Fe and Al oxides and oxyhydroxides (Kosmulski, 2009), the Fe and Al nanoparticles are likely to adsorb to the biotite surface between pH 3 and 7 due to the opposing surface charges. Therefore, the positive saturation indices likely indicate that Fe and Al phases may have precipitated during some of the closed system experiments, however these were only visible by scanning electron microscopy at pH 6 in the ligand-free experiments (Fig. S1D, CS-G19–21), and did not result in significant specific surface area changes in the post reaction samples (Table 1). These calculations highlight that the presence of organic ligands decreases secondary phase saturation, allowing the further release of Al and Fe into the fluid phase at a given pH, compared to the organic ligand-free experimental fluids.

The mechanism by which an organic ligand influences mineral dissolution has been described as complexation, either direct surface complexation or indirect solution based chelation and the associated effect on the solution affinity and/or activity of dissolution inhibitors, such as Al, (c.f. Drever and Stillings, 1997; Oelkers et al., 2001). In the case of biotite, it is likely that metal–ligand complexation occurs mainly in the fluid phase. In our previous study on the Grasåsen biotite (Bray et al., 2014) we demonstrated that the isoelectric point of biotite is at pH 3. Below this pH, the biotite surfaces have a net positive charge, above this pH, a net negative charge. Above pH 3 the dominant species of citric and oxalic acid are negatively charged such that interactions with the negatively charged biotite surface are likely limited. However, the dominant DFOB species in the range of pH of this study (2–6) is the positively charged H_4DFOB^+ species that might have been able to adsorb to biotite. However, although it has been demonstrated previously that the presence of DFOB promotes Al and Fe release to solution (Hersman et al., 1995; Holmén and Casey, 1996; Kraemer et al., 1999; Cocozza et al., 2002; Cheah et al., 2003; Kraemer, 2004; Buss et al., 2007; Reichard et al., 2007; ; Wolff-Boenisch and Traina, 2007a,b), its actual adsorption to the dissolving matrix has been discussed to be insufficient (3%) to account for the observed increase in dissolution rates, probably because of steric hindrance (Wolff-Boenisch and Traina, 2006).

4.2. Surface area and dissolution

The surface area normalised dissolution rates of the three Grasåsen biotite size fractions do not have a linear relationship with the total mineral surface area present in each experiment (SA_{BET} m^2, Fig. S5). This observation may stem from the anisotropic nature of the biotite surface reactivity (e.g., Turpault and Trotignon, 1994; Hodson, 2006). The logarithm of the dissolution rates appear to exhibit a linear correlation with the fraction of geometric specific surface attributed to the biotite edges ($hk0$, SA_{edge} %, Fig. S5, Table 1), demonstrating the importance of grain geometry on the overall dissolution rate. Like biotite, other sheet silicates have been shown to primarily dissolve parallel to the basal surface, i.e., at the ($hk0$) surfaces (Kaviratna and Pinnavaia, 1994; Turpault and Trotignon, 1994; Bosbach et al., 2000; Bickmore et al., 2001, 2003; Aldushin et al., 2006; Hodson, 2006; Saldi et al., 2007; Cappelli et al., 2013).

From the grain geometry measurements made using FEG-SEM (Fig. S1 and Table 1), the overall biotite dissolution rate constant at a single pH value (k'_{Si}, Eq. (2)) can be considered to be the sum of two contributions, in accord with (e.g., Hodson, 2006):

$$k'_{Si} = k'_{Si,edge} \cdot SA_{edge} + k'_{Si,basal} \cdot SA_{basal} \quad (6)$$

where $k'_{Si,edge}$ and $k'_{Si,basal}$ (moles m^{-2} s^{-q}) correspond to the rate constants of the dissolution of edge and basal surfaces respectively, and SA_{edge} and SA_{basal} designate the fraction of edge and basal surfaces of the total geometric surface area (Table 1). The values of $k'_{Si,edge}$ and $k'_{Si,basal}$ were obtained from extrapolating the linear regressions of k'_{Si} with SA_{edge} % and SA_{basal} % to 0 % SA_{basal} and SA_{edge}, respectively. At pH ~4 the value of $k'_{Si,edge}$ is 36.7×10^{-7} (moles m^{-2} s^{-q}), approximately 120 times greater than $k'_{Si,basal}$, 0.31×10^{-7} (moles m^{-2} s^{-q}, Table 5). The relative reactivities of the edge and basal surfaces calculated for the other elements also differ for edge or basal contributions. For example, the values of $k'_{Al,edge}$ and $k'_{Mg,edge}$ are 102 and 45 times greater than $k'_{Al,basal}$ and $k'_{Mg,basal}$, respectively. The relative reactivity of the edge and basal surfaces could not be calculated for Fe, as iron release was independent of grain geometry (Fig. S2B). These calculations, although limited due to the need to extrapolate experimental data, suggest that the relative reactivities are element specific, as observed previously (Turpault and Trotignon, 1994; Malmström and Banwart, 1997). Nevertheless, the calculated relative reactivity ratios of ($hk0$):(001) for each element (excluding Fe) fall within the range given by Turpault and Trotignon (1994) of 30–300, and Hodson (2006) of 71–132. However, the range presented in this study is pH specific and considering that the studied biotite changes its surface properties (surface charge and composition) with pH (Bray et al., 2014), the surface reactivities,

Table 5
Relative reactivity of the edge and basal surfaces of the Grasåsen biotite.

	Grasåsen			
	Al	Fe	Mg	Si
k'_{edge}	9.70×10^{-6}	NC	1.02×10^{-5}	3.67×10^{-6}
k'_{basal}	9.55×10^{-8}		2.29×10^{-7}	3.07×10^{-8}
k'_{edge}/k'_{basal}	102		45	120

NC, Not Calculated. Iron release appeared to be independent of grain size and geometry due to supersaturation of the fluid phase with respect to iron oxyhydroxides.

both for basal and edge planes, will also invariably be affected.

The total concentration of a given element released from biotite into the fluid phase ($\boldsymbol{m'_{i,t}}$) is controlled by the portion of edge and basal surface in each particle size fraction, and is the sum of these two distinct contributions. The contributions of the edge and basal surfaces to the total released Si at pH ~4 is shown for each size fraction in Fig. 5, calculated as in Eq. (7):

$$\boldsymbol{m'_{i,t}} = \boldsymbol{m'_{edgei,t}} + \boldsymbol{m'_{basali,t}}$$
$$\boldsymbol{m'_{i,t}} = (k'_{edge} \cdot t^{q} \cdot SA_{edge}) + (k'_{basal} \cdot t^{q} \cdot SA_{basal}) \quad (7)$$

The symbols in Fig. 5 are the experimentally measured, surface area and stoichiometry normalised concentrations of Si for each size fraction: (A) 25–53, (B) 53–180, and (C) 180–500 μm (experiments CS-G07–15). The solid black line in Fig. 5A, B, and C is the modelled fit of the experimental data (Eq. 2), which is the sum of the modelled contribution from the edge (long dash) and basal (short dash) surfaces. When the modelled summed $\boldsymbol{m'_{Si}}$ values are plotted against the experimentally measured $\boldsymbol{m'_{Si}}$ values a good fit is achieved (Fig. 5D). It is worth noting that the values of k'_{edge} and k'_{basal} were calculated using a fixed average value of q (Eq. 1) as this parameter varies by 0.06 as a function of grain size for silicon (Table 2). However, the modelled concentrations (Eq. 7, Fig. 5) were calculated using the values for q provided in Table 2.

It is also worth noting that SSA_{geo} for each of the size fractions is significantly less than the corresponding SSA_{BET}. The ratio of SSA_{BET}/SSA_{geo}, or roughness factor (Wolff-Boenisch et al., 2004), for the Grasåsen biotite ranges between ~8 for the 25–53 μm size fraction and ~3

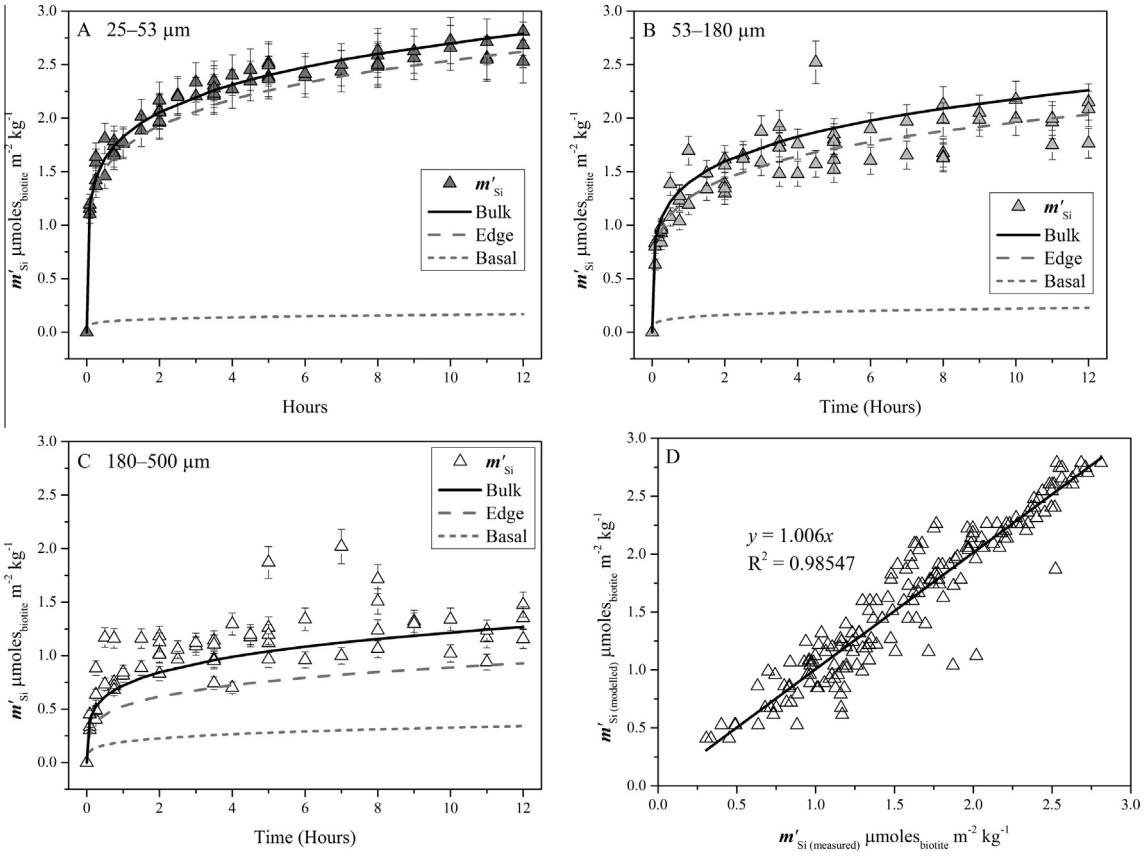

Fig. 5. Modelled element release from the bulk, edge and basal contributions for the three size fractions at pH ~4 in the Grasåsen biotite closed-system experiments, (A) 25–53 (experiments CS-G10–12), (B) 53–180 (experiments CS-G07–09), and (C) 180–500 (experiments CS-G13–15). The suitability of the model to represent experimental data was assessed through (D), where the 1:1 slope of the modelled concentrations against the experimental concentrations for these experiments is shown. Error bars represent the analytical uncertainty for silicon.

for the 180–500 μm size fraction. The biotite surface consists of relatively smooth basal surfaces and rough edges (see Fig. S1), so when the grains are predominantly free of smaller particles it follows that the roughness factor is directly linked to SA_{edge}. This also suggests that the values of SA_{edge} may underestimate the actual surface area present on the edge surfaces of biotite grains. If the SA_{edge} values were larger, then the calculated edge reactivity would be significantly lower.

The use of initial specific surface area for normalising phyllosilicate dissolution rates in 12 h closed-system experiments appears to be appropriate as there is minimal change in the specific surface area between pre- and post-reaction samples. The use of the initial surface area in experiments of longer duration, either closed- or open-system may not be appropriate for phyllosilicate dissolution studies.

4.3. Stoichiometry of dissolution

The stoichiometry of element release from the biotite structure during the first 12 h of reaction in the closed-system experiments can be assessed by plotting the stoichiometry and surface area normalised moles of each element released from biotite (m'_i) against the corresponding moles of Si (Fig. 6 and Fig. S6), and calculating the m'_i/m'_{Si} ratios (Table S5). In the organic ligand-free closed-system dissolution experiments the ratio of m'_{Al}/m'_{Si} (Fig. 6A) was pH independent and far from stoichiometric, revealing an average ratio of 2.2 (Standard Deviation, SD, 0.5). This non-stoichiometric release is also valid for the m'_{Fe}/m'_{Si} and m'_{Mg}/m'_{Si} (Fig. S6) ratios, which gave averages of 2.0 and 2.7, respectively (SD 0.8 and 0.6). It is worth noting that towards neutral pH the ratios of m'_{Al}/m'_{Si} and m'_{Fe}/m'_{Si} decrease (see insets of Fig. 6A and Fig. S6). At pH 6 the ratios for these elements are 1.04 and 0.48 respectively (SD 0.16 and 0.17), indicating near-stoichiometric release of Al and retention of Fe in the solid phase. This approach to stoichiometric Al release and Fe retention in the solid phase at pH 6 could be due to the precipitation of secondary Al and Fe oxy-hydroxide phases. In the all open-system Graså sen biotite experiments (Table S5), the ratio of m'_i/m'_{Si}, decreases during each experiment but in general remains greater than 1 after 300 h of reaction. Values reported in Table S5 are the average ratios during each experiment type. In one experiment at pH 3, the m'_{Al}/m'_{Si} ratio reached 0.7 after ~250 h. Non-stoichiometric release of structural metals has previously been described for biotite (Acker and Bricker, 1992; Turpault and Trotignon, 1994; Kalinowski and Schweda, 1996; Malmström and Banwart 1997).

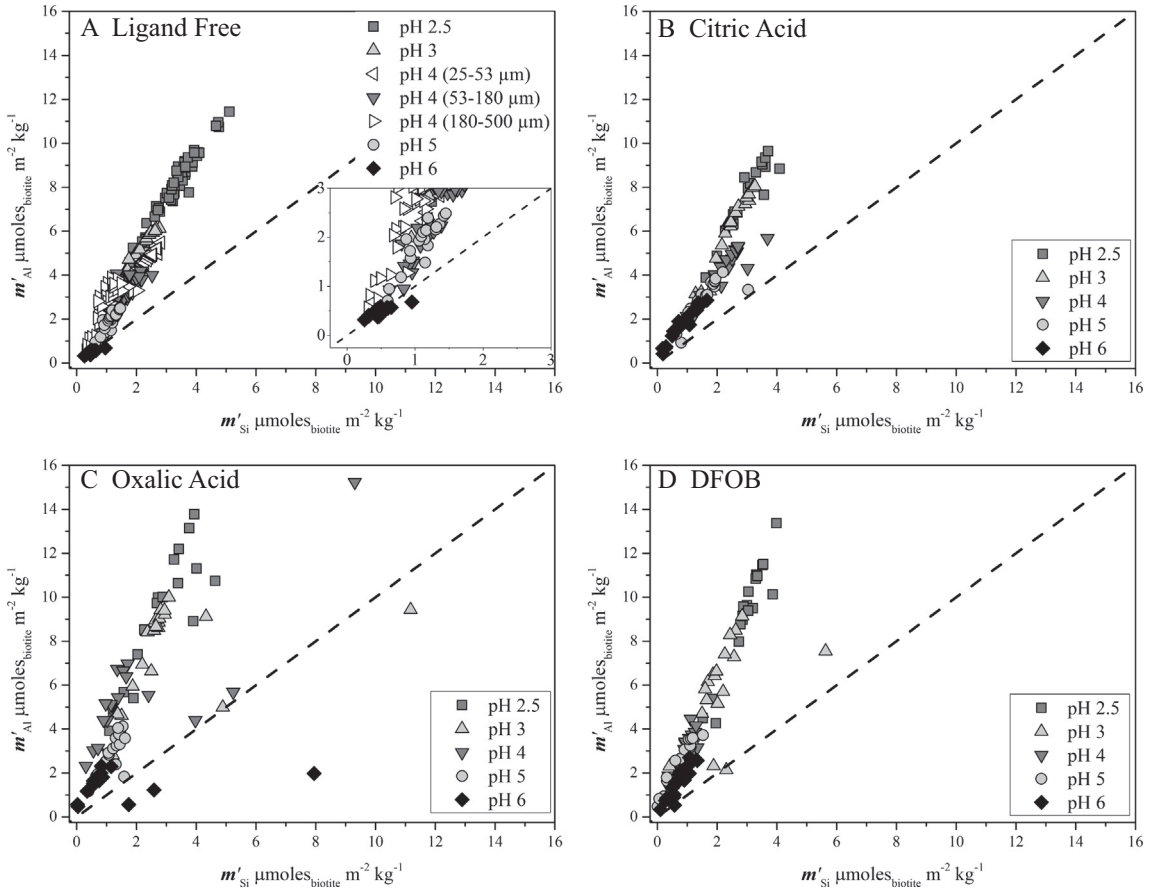

Fig. 6. Plots of released Al against released Si in the closed system experiments after reaction with (A) ligand-free, (B) citric acid, (C) oxalic acid, and (D) DFOB solutions. The dashed lines represent stoichiometric release and the inset in panel (A) highlights the lower region of the plot.

The $\boldsymbol{m}'_i/\boldsymbol{m}'_{Si}$ ratios from the closed-system experiments in the presence of organic ligands are presented in Fig. 6 and Fig. S6. In general, the $\boldsymbol{m}'_i/\boldsymbol{m}'_{Si}$ ratios increase in the presence of organic ligands with respect to the ligand-free experiments (Table S5). With citric acid, oxalic acid, or DFOB present in the experimental fluid the ratios for $\boldsymbol{m}'_{Al}/\boldsymbol{m}'_{Si}$ and $\boldsymbol{m}'_{Fe}/\boldsymbol{m}'_{Si}$ at pH 5 and 6 are more consistent with the respective ratios at lower pH (Fig 6 and Fig. S6). This enhanced release of metals in the presence of organic ligands likely stems from the increased solubility of Fe and Al (Fig. S4). These plots show that the presence of organic ligands allow the non-stoichiometry of biotite dissolution to be consistent from pH 2.5 to 6. The shift to stoichiometric dissolution observed for Al and Fe in the ligand-free experiments at higher pH does not occur in the presence of the organic ligands due to the decrease in saturation indices of secondary Fe and Al phases in the fluids.

4.4. Dissolution mechanism

In Bray et al. (2014) we demonstrated the formation of Mg and Fe depleted tetrahedral and Al depleted octahedral layers at the biotite surface at low pH. The average depth of this depleted layer was calculated from (Bray et al., 2014):

$$\mathrm{Dep}_i = \frac{\boldsymbol{m}'_i}{n_i\left(\frac{\rho_{\mathrm{biotite}}}{\boldsymbol{m}_{\mathrm{biotite}}}\cdot\frac{N}{10^{21}}\right)} \quad (8)$$

The average depth of removal of the ith element (Dep_i) was calculated by dividing the moles of the ith element removed from biotite during dissolution ($\boldsymbol{m}_i$) by the average density of atoms in the biotite structure (atoms nm^{-3}), where n_i is the stoichiometric coefficient of the ith element in the bulk biotite, ρ_{biotite} ($\mathrm{g\,cm}^{-3}$) represents the biotite density (3.09, average from webmineral.com), $\boldsymbol{m}_{\mathrm{biotite}}$ refers to the molecular mass of biotite ($450.15\ \mathrm{g\,mol}^{-1}$ for the Graså sen biotite), and N is Avogadro's constant ($6.022\times10^{23}\ \mathrm{moles}^{-1}$). Based on these assumptions we calculated depletion depths from the total moles of elements released, ignoring the relative reactivities of the basal (0 0 1) and edge ($hk0$) surfaces. Combining this information with the dissolution data from this study we can also calculate the depth of element removal from biotite from both the basal (0 0 1) and edge ($hk0$) planes. This can be done by replacing $\boldsymbol{m}'_i$ in Eq. (8) with the released moles of elements from the basal and edge surfaces ($\boldsymbol{m}'_{\mathrm{edge},i}$ and $\boldsymbol{m}'_{\mathrm{basal},i}$, Eq. 7). To visualise these removal fronts during biotite dissolution for each element, on the more reactive edge surfaces, at the various pH values and both in the presence and absence of organic ligands schematics showing dissolution fronts

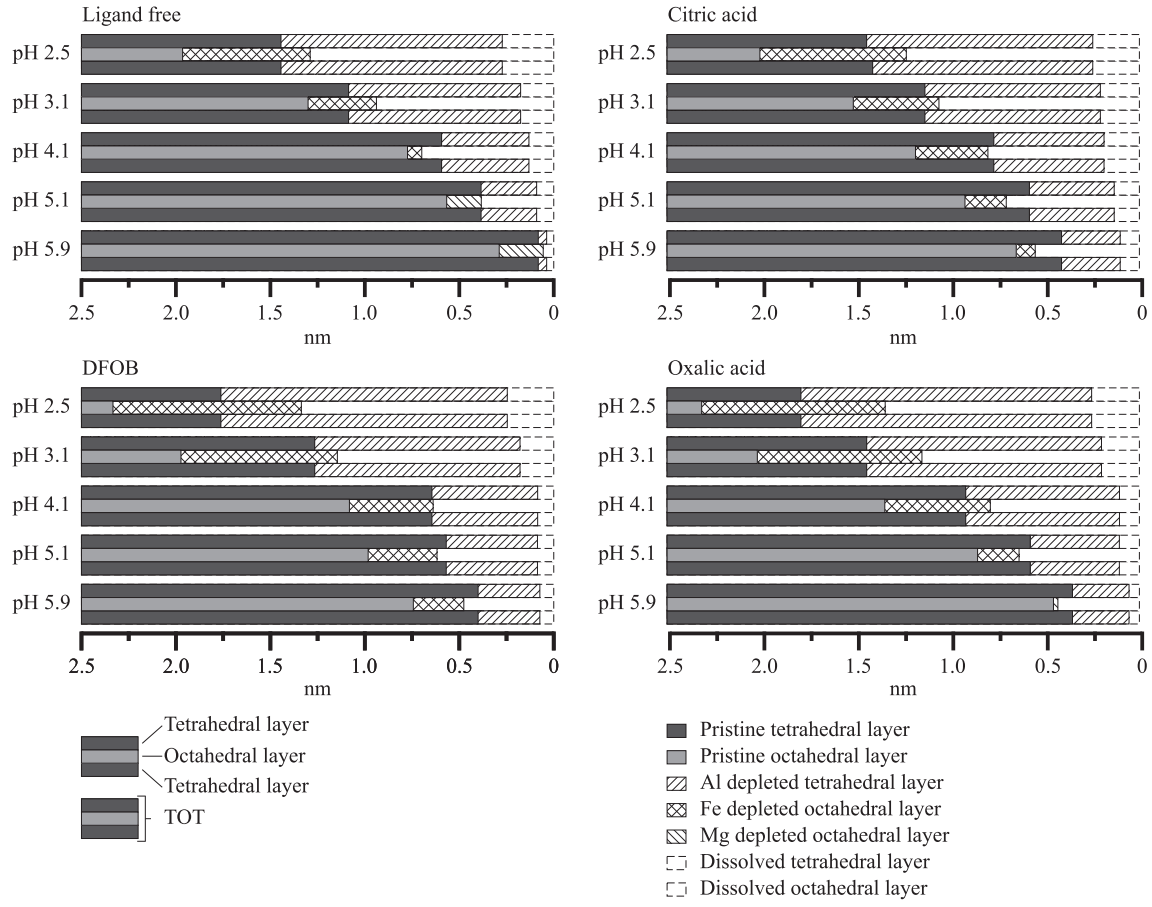

Fig. 7. Calculated depths of dissolution fronts in the tetrahedral and octahedral layers as a function of pH and organic ligand. Calculations based on the reactivity of ($hk0$) and released concentrations after 12 h.

linked to tetrahedral and octahedral layers were plotted in Fig. 7. We have shown (Table 5) that the edge surfaces are 120 times more reactive than the basal surfaces and thus the majority of dissolution occurs perpendicular to the (0 0 1) plane. The extent of element removal from biotite after 12 h as a function of pH and presence of organic ligands based on released element concentrations were attributed to either tetrahedral or octahedral sites depending on the biotite structure. At all pH in both organic ligand bearing and ligand-free experiments, octahedral metal (Fe, Mg) release was faster than tetrahedral element (Al and Si) release, consistent with numerous multi-oxide silicates (c.f. Oelkers et al., 2009). In the organic ligand-free experiments, Fe was preferentially released over Mg from the octahedral layer at pH 2.5–4, whereas at pH 5 and 6, Fe was preferentially retained over Mg. This change in element release is likely due to the control of secondary phase equilibria on Fe release above pH 5, where Fe-oxyhydroxide solubility is low. It is unclear from these experiments, therefore, if Fe retention was within the biotite structure or as a secondary mineral precipitate (in Fig. 7 it is represented as in the biotite structure) as in almost all experiments no quantitative microscopic evidence of secondary mineral formation is available. The preferential retention of Fe in the solid phase at near neutral conditions was observed in the presence of oxalic acid only at pH 6 (Fig. 7), but not in the presence of citric acid or DFOB at any pH, probably due to their effect on increasing Fe solubility. It is also likely that during dissolution, $Fe^{(II)}$ oxidation within the biotite structure occurs. Such a process has been shown to lead to the formation of $Fe^{(III)}$ subdomains (Bonneville et al., 2009); however, the quantification of changes in the Fe oxidation states in the biotite samples was not quantified in this study. Similarly, the release of Al from tetrahedral sites in the presence of organic ligands was greatly increased compared to the ligand-free experiments above pH 3. The depth of Al removal at pH 6 in the presence of organic ligands was approximately 2.5 times greater than in the ligand-free experiments. Biotite dissolution is known to proceed non-stoichiometrically (Kalinowski and Schweda, 1996; Malmström et al., 1996; Malmström and Banwart, 1997; Voinot et al., 2013; Bray et al., 2014), however Acker and Bricker (1992) suggested that the dissolution of octahedral and tetrahedral layers can be internally stoichiometric, i.e., Fe and Mg release from the octahedral layer could be stoichiometric but overall this could be non stoichiometric compared to the bulk chemistry. Fig. 7 also demonstrates that for the Grasåsen biotite, this is not the case. Indeed, Mg and Fe release from the octahedral layer was not stoichiometric and similarly Al and Si release from the tetrahedral layer was also non stoichiometric.

5. CONCLUSION

The results summarised above illustrate the complex, but systematic dissolution behaviour of biotite, a common sheet silicate mineral. Dissolution is dominated by the biotite edges, which are between 45 and 120 times more reactive than the basal surface. Dissolution at these edges at acidic conditions occurs via the independent removal of the cations at distinct rates, where Mg and Fe are in general released faster than Al, which itself is released faster than Si. As a result, with time the biotite edges change composition and structure, the outermost edge consisting of an Al depleted tetrahedral framework adjacent to a Mg, Fe depleted octahedral layer. Deeper into the biotite, increasing Al, Mg, and Fe are present until a stoichiometric biotite is found deep within the grains. As rates are dominated by removal of material from edge surfaces, which constitute only a small fraction of the total biotite surface area, the degree to which total surface area normalised rates can represent natural processes is questionable.

Calculated dissolution rates from closed-system experiments converge with steady state dissolution rates derived from open-system experiments after approximately 12 h of reaction. The stoichiometry and surface area normalised dissolution rates of the Grasåsen and Moen biotites are largely consistent with existing data. However, the apparent rate constants calculated for biotite samples of differing chemical composition vary between elements, indicating element specific rates which could be described by element specific rate laws.

The presence of organic ligands, at low concentrations, enhanced the release of di- and tri-valent metals from both octahedral and tetrahedral layers, compared to ligand-free experiments. This was likely facilitated by the formation of metal–organic ligand complexes, driving the system equilibrium to promote further release of, in particular, Al and Fe. As such the relatively low concentrations of organic ligands considered in this study, similar to concentrations known to be exuded by microorganisms, increase the release rates of important secondary nutrients (Al, Fe, and Mg) from biotite. However, this increased release of metals did not significantly influence the biotite dissolution rate, based on Si release, as element reactivities and dissolution rates in biotite appear to be largely independent.

ACKNOWLEDGEMENTS

This study was enabled by funding from the UK Natural Environment Research Council Weathering Science Consortium (NE/C004566/1) and The Geological Society of London William George Fearnsides Fund, both of which the authors are extremely grateful for. The authors acknowledge Tor Sigvald Johansen of the Agder Naturmuseum, Kristiansand, Norway, for providing the Grasåsen biotite sample. The authors would also like to acknowledge members of Cohen Geochemistry (Univ. Leeds), the Hydrogeochemistry group (Univ. Iceland), and Géosciences Environnement Toulouse (CNRS) for their support. Particular thanks go to Andrew Kilpatrick, Jörgen Rosenqvist, Snorri Gudbrandsson, Helgi A. Alfreðsson, Julien Declercq, Vassilis Mavromatis, Chiara Cappelli, Ian Burke, and Mark Hodson for useful discussions through the course of this study.

APPENDIX A. SUPPLEMENTARY DATA

Supplementary data associated with this article can be found, in the online version, at http://dx.doi.org/10.1016/j.gca.2015.04.048.

REFERENCES

Acker J. G. and Bricker O. P. (1992) The influence of pH on biotite dissolution and alteration kinetics at low temperature. *Geochim. Cosmochim. Acta* **56**, 3073–3092.

Adeyemi A. O. and Gadd G. M. (2005) Fungal degradation of calcium-, lead- and silicon-bearing minerals. *Biometals* **18**, 269–281.

Aldushin K., Jordan G. and Schmahl W. W. (2006) Basal plane reactivity of phyllosilicates studied in situ by hydrothermal atomic force microscopy (HAFM). *Geochim. Cosmochim. Acta* **70**, 4380–4391.

Arvidson R. S. and Lüttge A. (2010) Mineral dissolution kinetics as a function of distance from equilibrium – new experimental results. *Chem. Geol.* **269**, 79–88.

Balland C., Poszwa A., Leyval C. and Mustin C. (2010) Dissolution rates of phyllosilicates as a function of bacterial metabolic diversity. *Geochim. Cosmochim. Acta* **74**, 5478–5493.

Balogh-Brunstad Z., Keller C. K., Dickinson J. T., Stevens F., Li C. Y. and Bormann B. T. (2008) Biotite weathering and nutrient uptake by ectomycorrhizal fungus, *Sillus tomentosis*, in liquid-culture experiments. *Geochim. Cosmochim. Acta* **72**, 2601–2618.

Beerling D. J. and Berner R. A. (2005) Feedbacks and the coevolution of plants and atmospheric CO_2. *PNAS* **102**, 1302–1305.

Berner E. K. and Berner R. A. (1996) *Global Environment: Water, Air and Geochemical Cycles*. Prentice Hall.

Bickmore B. R., Bosbach D., Hochella M. F., Charlet L. and Rufe E. (2001) In situ atomic force microscopy study of hectorite and nontronite dissolution: Implications for phyllosilicate edge surface structures and dissolution mechanisms. *Am. Mineral.* **86**, 411–423.

Bickmore B. R., Rosso K. M., Nagy K. L., Cygan R. T. and Tadanier C. J. (2003) *Ab initio* determination of edge surface structures for dioctahedral 2:1 phyllosilicates: implications for acid–base reactivity. *Clays Clay Miner.* **51**, 359–371.

Bonneville S., Smits M. M., Brown A., Harrington J., Leake J. R., Brydson R. and Benning L. G. (2009) Plant-driven fungal weathering: early stages of mineral alteration at the nanometer scale. *Geology* **37**, 615–618.

Bonneville S., Morgan D. J., Schmalenberger A., Bray A., Brown A., Banwart S. A. and Benning L. G. (2011) Tree-mycorrhiza symbiosis accelerate mineral weathering: evidences from nanometer-scale elemental fluxes at the hypha-mineral interface. *Geochim. Cosmochim. Acta* **75**, 6988–7005.

Bosbach D., Charlet L., Bickmore B. and Jr Hochella. M. F. (2000) The dissolution of hectorite: in-situ, real-time observations using atomic force microscopy. *Am. Mineral.* **85**, 1209–1216.

Bowser C. J. and Jones B. F. (2002) Mineralogic controls on the composition of natural waters dominated by silicate hydrolysis. *Am. J. Sci.* **302**, 582–662.

Brantley S. L. (2003) Reaction kinetics of primary rock-forming minerals under ambient conditions. In *Surface and Ground Water, Weathering, and Soils*, vol. 5 (ed. J. I. Drever) (eds. H. D. Holland and K. K. Turekian). Elsevier-Pergamon, Oxford, pp. 73–118.

Bray A. W., Benning L. G., Bonneville S. and Oelkers E. H. (2014) Biotite surface chemistry as a function of aqueous fluid composition. *Geochim. Cosmochim. Acta* **128**, 58–70.

Brunauer S., Emmett P. H. and Teller E. (1938) Adsorption of gases in multimolecular layers. *J. Am. Chem. Soc.* **60**, 309–319.

Buss H. L., Lüttge A. and Brantley S. L. (2007) Etch pit formation on iron silicate surfaces during siderophore-promoted dissolution. *Chem. Geol.* **240**, 326–342.

Cappelli C., Van Driessche A. E. S., Cama J. and Huertas F. J. (2013) In situ observation of biotite dissolution at pH 1 using advanced optical microscopy. *Cryst. Growth Des.* **13**, 2880–2886.

Chaïrat C., Schott J., Oelkers E. H., Lartigue J.-E. and Harouiya N. (2007) Kinetics and mechanism of natural fluorapatite dissolution at 25 °C and pH 3 to 12. *Geochim. Cosmochim. Acta* **71**, 5901–5912.

Cheah S.-F., Kraemer S. M., Cervini-Silva J. and Sposito G. (2003) Steady-state dissolution kinetics of goethite in the presence of desferrioxamine B and oxalate ligands: implications for the microbial acquisition of iron. *Chem. Geol.* **198**, 63–75.

Cocozza C., Tsao C. C. G., Cheah S.-F., Kraemer S. M., Raymond K. N., Miano T. M. and Sposito G. (2002) Temperature dependence of goethite dissolution promoted by trihydroxamate siderophores. *Geochim. Cosmochim. Acta* **66**, 431–438.

Davis J. A. and Kent D. B. (1990) Surface complexation modelling in aqueous geochemistry. *Rev. Mineral. Geochem.* **23**, 117–260.

Declercq J., Bosc O. and Oelkers E. H. (2013) Do organic ligands affect forsterite dissolution rates?. *Appl. Geochem.* **39** 69–77.

Drever J. I. (1997) *The Geochemistry of Natural Waters*, third ed. Prentice-Hall, New Jersey, 436.

Drever J. I. and Stillings L. L. (1997) The role of organic acids in mineral weathering. *Colloids Surf., A* **120**, 167–181.

Flaathen T. K., Gislason S. R. and Oelkers E. H. (2010) The effect of aqueous sulphate on basaltic glass dissolution rates. *Chem. Geol.* **277**, 345–354.

Fischer C., Kurganskaya I., Schäfer T. and Lüttge A. (2014) Variability of crystal surface reactivity: what do we know? *Appl. Geochem.* **43**, 132–157.

Gautelier M., Schott J. and Oelkers E. H. (2007) An experimental study of dolomite dissolution rates at 80 °C as a function of chemical affinity and solution composition. *Chem. Geol.* **242**, 509–517.

Gazzè S. A., Saccone L., Ragnarsdóttir K. V., Smits M. M., Duran A. L., Leake J. R., Banwart S. A. and McMaster T. J. (2012) Nanoscale channels on ectomycorrhizal-colonized chlorite: evidence for plant-driven fungal dissolution. *J. Geophys. Res.* **117**, G00N09.

Gazzè S. A., Saccone L., Smits M. M., Duran A. L., Leake J. R., Banwart S. A., Ragnarsdottir K. V. and McMaster T. J. (2013) Nanoscale observations of extracellular polymeric substances deposition on phyllosilicates by an ectomycorrhizal fungus. *Geomicrobiol J.* **30**, 721–730.

Golubev S. V. and Pokrovsky O. S. (2006) Experimental study of the effect of organic ligands on diopside dissolution kinetics. *Chem. Geol.* **235**, 377–389.

Golubev S. V., Bauer A. and Pokrovsky O. S. (2006) Effect of pH and organic ligands on the kinetics of smectite dissolution at 25 °C. *Geochim. Cosmochim. Acta* **70**, 4436–4451.

He Y. T., Bigham J. M. and Traina S. J. (2005) Biotite dissolution and Cr(VI) reduction at elevated pH and ionic strength. *Geochim. Cosmochim. Acta* **69**, 3791–3800.

Hersman L., Lloyd T. and Sposito G. (1995) Siderophore-promoted dissolution of hematite. *Geochim. Cosmochim. Acta* **59**, 3327–3330.

Hodson M. E. (2006) Does reactive surface area depend on grain size? Results from pH 3, 25 °C far-from-equilibrium flow-through experiments on anorthite and biotite. *Geochim. Cosmochim. Acta* **70**, 1655–1667.

Holmén B. A. and Casey W. H. (1996) Hydromamate ligands, surface chemistry, and the mechanism of ligand-promoted dissolution of goethite [α-FeOOH(s)]. *Geochim. Cosmochim. Acta* **60**, 4403–4416.

Hopf J., Langenhorst F., Pollok K., Merten D. and Kothe E. (2009) Influence of microorganisms on biotite dissolution: an experimental approach. *Chem. Erde* **69**, 45–56.

Jones D. L. (1998) Organic acids in the rhizosphere – a critical review. *Plant Soil* **205**, 25–44.

Kalinowski B. E. and Schweda P. (1996) Kinetics of muscovite, phlogopite and biotite dissolution and alteration at pH 1–4, room temperature. *Geochim. Cosmochim. Acta* **60**, 367–385.

Kaviratna H. and Pinnavaia T. J. (1994) Acid hydrolysis of octahedral Mg^{2+} sites in 2:1 layered silicates: an assessment of edge attack and gallery access mechanisms. *Clays Clay Miner.* **42**, 717–723.

Köhler S. J., Harouiya N., Chaïrat C. and Oelkers E. H. (2005) Experimental studies of REE fractionation during water–mineral interactions: REE release rates during apatite dissolution from pH 2.8 to 9.2. *Chem. Geol.* **222**, 168–182.

Kosmulski M. (2009) Compilation of PZC and IEP of sparingly soluble metal oxides and hydroxides from literature. *Adv. Colloid Interface Sci* **152**, 14–25.

Kraemer S. M. (2004) Iron oxide dissolution and solubility in the presence of siderophores. *Aquat. Sci.* **66**, 3–18.

Kraemer S. M., Cheah S.-F., Zapf R., Xu J., Raymond K. N. and Sposito G. (1999) Effect of hydroxamate siderophores on Fe releases and Pb(II) adsorption by goethite. *Geochim. Cosmochim. Acta* **63**, 3003–3008.

Lapeyrie F. (1988) Oxalate synthesis from soil bicarbonate by the mycorrhizal fungus *Paxillus involutus*. *Plant Soil* **110**, 3–8.

Lapeyrie F., Chilvers G. A. and Bhem C. A. (1987) Oxalic acid synthesis by the mycorrhizal fungus *Paxillus involutus* (Batsch. ex Fr.) Fr. *New Phytol.* **106**, 139–146.

Lasaga A. C. (1998) *Kinetic Theory in the Earth Sciences*. Princeton University Press, NJ.

Martell A. E. and Smith R. M. (1977) *Critical Stability Constants: Volume 3 Other Organic Ligands*. Springer, New York.

Martell A. E., Smith R. M. and Motekaitis R. J. (2004) NIST critically selected stability constants, Standard Reference Database 46, version 8.0.

Malmström M. and Banwart S. (1997) Biotite dissolution at 25 °C: the pH dependence of dissolution rate and stoichiometry. *Geochim. Cosmochim. Acta* **61**, 2779–2799.

Malmström M., Banwart S., Lewenhagen J., Duro L. and Bruno J. (1996) The dissolution of biotite and chlorite at 25 °C in the near-neutral pH region. *J. Contam. Hydrol.* **21**, 201–213.

Nesbitt H. W. and Young G. M. (1984) Prediction of some weathering trends of plutonic and volcanic rocks based on thermodynamic and kinetic considerations. *Geochim. Cosmochim. Acta* **48**, 1523–1534.

Oelkers E. H. and Gislason S. R. (2001) The mechanism, rates and consequences of basaltic glass dissolution: I. An experimental study of the dissolution rates of basaltic glass as a function of aqueous Al, Si and oxalic acid concentration at 25 °C and pH = 3 and 11. *Geochim. Cosmochim. Acta* **65**, 3671–3681.

Oelkers E. H. and Schott J. (2001) An experimental study of enstatite dissolution rates as a function of pH, temperature, and aqueous Mg and Si concentration, and the mechanism of pyroxene/pyroxenoid dissolution. *Geochim. Cosmochim. Acta* **65**, 1219–1231.

Oelkers E. H., Schott J. and Devidal J.-L. (2001) On the interpretation of closed system mineral dissolution experiments: comment on "Mechanism of kaolinite dissolution at room temperature and pressure Part II: Kinetic study" by Huertas et al. (1999). *Geochim. Cosmochim. Acta* **65**, 4429–4432.

Oelkers E. H., Schott J., Gauthier J.-M. and Herrero-Roncal T. (2008) An experimental study of the dissolution mechanism and rates of muscovite. *Geochim. Cosmochim. Acta* **72**, 4948–4961.

Oelkers E. H., Golubev S. V., Chairat C., Pokrovsky O. S. and Schott J. (2009) The surface chemistry of multi-oxide silicates. *Geochim. Cosmochim. Acta* **73**, 4617–4634.

Parkhurst D. L. and Appelo C. A. J., (2013) PHREEQC version 3 – A computer program for speciation, batch-reaction, one-dimensional transport, and inverse geochemical calculations. Available from: <http://wwwbrr.cr.usgs.gov/projects/GWC_coupled/phreeqc/>.

Reichard P. U., Kretzschmar R. and Kraemer S. M. (2007) Dissolution mechanisms of goethite in the presence of siderophores and organic acids. *Geochim. Cosmochim. Acta* **71**, 5635–5650.

Rimstidt J. D. (2014) *Geochemical Rate Models. An Introduction to Geochemical Kinetics*. Cambridge University Press, Cambridge, UK.

Saccone L., Gazzè S. A., Duran A. L., Leake J. R., Banwart S. A., Ragnarsdóttir K. V., Smits M. M. and McMaster T. J. (2012) High resolution characterization of ectomycorrhizal fungal–mineral interactions in axenic microcosm experiments. *Biogeochemistry* **111**, 411–425.

Saldi G. D., Köhler S. J., Marty N. and Oelkers E. H. (2007) Dissolution rates of talc as a function of solution composition, pH and temperature. *Geochim. Cosmochim. Acta* **71**, 3446–3457.

Saldi G. D., Schott J., Pokrovsky O. S. and Oelkers E. H. (2010) An experimental study of magnesite dissolution rates at neutral to alkaline conditions and 150 and 200 °C as a function of pH, total dissolved carbonate concentrations, and chemical affinity. *Geochim. Cosmochim. Acta* **74**, 6344–6356.

Schott J., Pokrovsky O. S. and Oelkers E. H. (2009) The link between mineral dissolution/precipitation kinetics and solution chemistry. *Rev. Mineral. Geochem.* **70**, 207–258.

Schott J., Pokrovsky O. S., Spalla O., Devreux F., Gloter A. and Mielczarski J. A. (2012) Formation, growth and transformation of leached layers during silicate minerals dissolution: the example of wollastonite. *Geochim. Cosmochim. Acta* **98**, 259–281.

Sposito G. (1984) *The Surface Chemistry of Soils*. Oxford University Press, New York, 234.

Stockmann G. J., Wolff-Boenisch D., Gislason S. R. and Oelkers E. H. (2013) Do carbonate precipitates affect dissolution kinetics?: 2: Diopside. *Chem. Geol.* **337–338**, 56–66.

Taylor L. L., Leake J. R., Quirk J., Hardy K., Banwart S. A. and Beerling D. J. (2009) Biological weathering and the long-term carbon cycle: integrating mycorrhizal evolution and function into the current paradigm. *Geobiology* **7**, 171–191.

Turpault M. P. and Trotignon L. (1994) The dissolution of biotite single crystals in dilute HNO_3 at 24 °C; evidence of an anisotropic corrosion process of micas in acidic solution. *Geochim. Cosmochim. Acta* **58**, 2761–2775.

Ullman W. J. and Welch S. A. (2002) Organic ligands and fields dissolution. In *Water–Rock Interactions, Ore Deposits, and Environmental Geochemistry* (eds. Hellman and Wood). The Geochemical Society, pp. 3–35.

Voinot A., Lemarchand D., Collignon C., Granet M., Chabaux F. and Turpault M.-P. (2013) Experimental dissolution vs. transformation of micas under acidic soil conditions: clues from boron isotopes. *Geochim. Cosmochim. Acta* **117**, 144–160.

Wolff-Boenisch D. and Traina S. J. (2006) A comparative study of the effect of desferrioxamine B, oxalic acid, and Na-alginate on the desorption of U(VI) from goethite at pH 6 and 25 °C. *Geochim. Cosmochim. Acta* **70**, 4356–4366.

Wolff-Boenisch D. and Traina S. J. (2007a) The effect of desferrioxamine B on the desorption of U(VI) from Georgia kaolinite KGa-1b and its ligand-promoted dissolution at pH 6 and 25 °C. *Chem. Geol.* **242**, 278–287.

Wolff-Boenisch D. and Traina S. J. (2007b) The effect of desferrioxamine B, enterobactin, oxalic acid, and Na-alginate on the dissolution of uranyl-treated goethite at pH 6 and 25 °C. *Chem. Geol.* **243**, 357–368.

Wolff-Boenisch D., Gislason S. R., Oelkers E. H. and Putnis C. V. (2004) The dissolution rates of natural glasses as a function of their composition at pH 4 and 10.6 and temperatures from 25 to 74 °C. *Geochim. Cosmochim. Acta* **68**, 4843–4858.

Wolff-Boenisch D., Wenau S., Gislason S. R. and Oelkers E. H. (2011) Dissolution of basalts and peridotite in seawater, in the presence of ligands, and CO_2: implications for mineral sequestration of carbon dioxide. *Geochim. Cosmochim. Acta* **75**, 5510–5525.

Zhang L. and Lüttge A. (2009) Morphological evolution of dissolving feldspar particles with anisotropic surface kinetics and implications for dissolution rate normalization and grain size dependence. A kinetic modelling study. *Geochim. Cosmochim. Acta* **73**, 6757–6770.

Associate editor: John Moreau